Available online at www.sciencedirect.com
SCIENCE DIRECT®
Geochimica et Cosmochimica Acta 70 (2006) 1710–1727
Geochimica
www.elsevier.com/locate/gca

Iron-oxide crystallinity increases during soil redox oscillations

Aaron Thompson [a], Oliver A. Chadwick [b], Denis G. Rancourt [c], Jon Chorover [a,*]

[a] Department of Soil, Water and Environmental Science, University of Arizona, Tucson, AZ 85721, USA
[b] Department of Geography, University of California, Santa Barbara, CA 93106, USA
[c] Department of Physics, University of Ottawa, Ottawa, Ont., Canada K1N 5N6

Received 25 April 2005; accepted in revised form 9 December 2005

Abstract

An Inceptisol A-horizon from Hawaii was subjected to a series of reduction-oxidation cycles—14 d cycle length over a 56 d duration—across the "soil-Fe" [$Fe(OH)_3.Fe^{2+}_{(aq)}$, $\log K^o = 15.74$] equilibrium in triplicate redox-stat reactors. Each reducing event simulated the flush of organic C and diminished O_2 that accompanies a rainfall-induced leaching of bioavailable reductants from the forest floor into mineral soil. The soil contained considerable amounts of short-range ordered (SRO) minerals (e.g., nano-goethite and allophane) and organic matter (11% org-C). Room temperature and cryogenic ^{57}Fe Mössbauer spectroscopy showed that the iron-bearing minerals were dominated by nano- to micro-scale goethite, and that ferrihydrite was not present. Over the four full cycles, fluctuations in E_h (from 200 to 700 mV) and pFe^{2+} (from 2.5 to 5.5) were inversely correlated with those of pH (5.5 to 4). Here, we focus on the solubility dynamics of the framework elements (Si, Fe, Ti, and Al) that constitute 35% of the oxygen-free soil dry mass. Intra-cycle oscillations in dissolved (<3 kDa) metals peaked during the reduction half-cycles. Similar intra-cycle oscillations were observed in the HCl and acid ammonium oxalate (AAO) extractable pools. The cumulative response of soil solids during multiple redox oscillations included: (1) a decrease in most HCl and AAO extractable metals and (2) a transformation of SRO Fe (as nano-goethite) to micro-crystalline goethite and micro-crystalline hematite. This may be the first direct demonstration that Fe oxide crystallinity *increases* during redox oscillations—an a priori unexpected result.

1. Introduction

An array of Fe-oxides, ranging from short range ordered (SRO; e.g., ferrihydrite, $Fe_5HO_8 \cdot 4H_2O$) to long-range ordered (e.g., well-crystallized goethite, α-FeOOH; hematite, α-Fe_2O_3; or magnetite, Fe_3O_4), coexist in a given soil because of kinetic constraints on mineral transformations and open system fluctuations in geochemical conditions. These solids present reactive interfaces for sorption and transformation of aqueous species. They are also subjected to microbially catalyzed reductive dissolution (i.e., bioreduction) when molecular oxygen becomes depleted in the presence of organic matter, which can result in solubilization of bound constituents. Fe bioreduction rates are controlled by oxide surface area (Roden, 2003) and thermodynamic solubility (Bonneville et al., 2004). Upon reintroduction of O_2, Fe^{II} is re-oxidized rapidly, resulting in the neoformation of Fe-oxides that can scavenge organic acids, metal cations and oxyanions from the soil solution. Thus, Fe redox transformations can have a profound influence on soil biogeochemistry.

In many environments, such as rooting zones of wetland plants (Flessa and Fischer, 1992; King and Garey, 1999) or sediments in near-shore environments affected by bioturbation (Aller, 1994), Fe oxidation state is subjected to temporal oscillations (Reddy et al., 1989; Van Cappellen et al., 1998). Similarly, when upland forest soils undergo periodic O_2 depletion (particularly in soil aggregates) in concert with rainfall, leaching of labile organic matter (OM) from the forest floor can lead to dynamic oscillations in soil redox status (Silver et al., 1999; Schuur and Matson, 2001). These redox-dynamic environments typically have high rates of biological activity and their geochemical influence

* Corresponding author. Fax: +1 520 621 1647.
E-mail address: Chorover@cals.arizona.edu (J. Chorover).

0016-7037/$ - see front matter © 2005 Elsevier Inc. All rights reserved.
doi:10.1016/j.gca.2005.12.005

extends into adjacent "redox-static" regions (Van Cappellen et al., 1998; Komada et al., 2004). Although iron is observed to undergo repeated transitions between Fe^{III} and Fe^{II} in such systems (Aller et al., 1986; Van Cappellen et al., 1998; Anschutz et al., 2000), the cumulative effects of such cycling are not known.

In most soils, Fe^{III}, in the form of kinetically reducible (i.e., "labile") oxides, is the largest contributor to soil oxidation capacity when O_2 is absent (Kirk, 2004). Thus, soils undergoing temporary oxygen depletion will be poised within the pH–pE range corresponding to Fe reduction as Fe^{II} accumulates in the soil solution or in mixed valence oxides such as magnetite ($Fe^{III}{}_2Fe^{II}O_4$). Upon re-introduction of O_2, rapid precipitation of Fe^{III} into hydrous oxides ensues because of supersaturation. The incipient product of Fe^{II} oxidation is expected to be short-range-ordered (SRO) Fe^{III}-oxides such as ferrihydrite, because such hydrated solids typically exhibit low interfacial energies of nucleation (Stumm and Morgan, 1996). When the oxidation occurs under low dissolved oxygen (DO) conditions and in the presence of organic acids, aqueous organic–Fe^{III} complexes can also form (Liang et al., 1993; Pullin and Cabaniss, 2003) as well as disordered, organic-poisoned versions of ferrihydrite (Rancourt et al., 2005). Under sustained oxidizing conditions, Ostwald ripening is expected to spawn a time-dependent increase in the degree of crystal ordering of minerals that coincides with their diminished aqueous solubility (Steefel and Van Cappellen, 1990). Thus, current understanding suggests that oxidative supersaturation of organic-rich soil solutions will favor initially the formation of aqueous organic–Fe complexes and amorphous solids (i.e., SRO Fe-oxides) rather than well-ordered Fe-oxides. Subsequent onset of reducing conditions can be expected to preferentially dissolve SRO Fe-oxides, but also more crystalline varieties (e.g., goethite) to some smaller degree (Bonneville et al., 2004; Roden, 2004). Thus, repeated redox oscillations are predicted to promote the accumulation of SRO Fe-oxides as they are the primary predicted products formed during the oxidizing half-cycles.

The objective of this research was to assess the influence of multiple Fe redox oscillations on the dissolution–precipitation behavior of Fe and on associated elements in a complex natural soil system. A complete Fe redox cycle is defined here to comprise the transition from Fe^{III} to Fe^{II} and back to Fe^{III}. We postulated that consecutive Fe redox cycles would result in long-term behavior that differed from that observed in a single cycle, particularly with respect to the relative predominance of Fe-bearing solids. Specifically, we hypothesized that oscillation in Fe redox status would promote: (1) the accumulation of metastable SRO Fe-oxides and (2) lead to progressively greater rates of Fe reduction. The approach was to force systematic redox oscillations on stirred soil suspensions while applying a comprehensive geochemical sampling protocol. This approach has not been applied previously to the study of Fe redox cycling.

2. Materials and methods

2.1. Overall approach

Prior methods for examining/describing redox-fluctuating environments include extrapolating from knowledge of oxic and anoxic end-members (Cornell and Schwertmann, 1996), forcing intermediate redox conditions using E_h-stat reactors (Patrick et al., 1973), documenting the biogeochemical changes during a single transition between oxic and anoxic conditions (Patrick and Jugsujinda, 1992; Brennan and Lindsay, 1998), making microscale field measurements across the oxic/anoxic interface (Frenzel et al., 1999; Zhang and Pang, 1999; Anschutz et al., 2000), or segregating (spatially) oxic and anoxic regions to create an identifiable interface (Roden et al., 2004). Our approach is a variant of prior experimental designs employing alternating anoxic/oxic atmospheres (Reddy and Patrick, 1975; Aller, 1994; Caradec et al., 2004). We specifically target Fe valence state transitions using a "soil-Fe":Fe^{II} (Lindsay, 1979) equilibrium model to define progressive E_h-triggered additions of air during the oxidizing half-cycle and real-time DOC measurements to define C additions during the reducing half-cycles.

2.2. Soil selection

A soil was selected from a well-characterized climate gradient on the island of Maui, HI that had shown documented E_h fluctuations (based on field measurements) that span the solubility range of several Fe-oxides (Chadwick and Chorover, 2001; Miller et al., 2001; Schuur and Matson, 2001). The soil contains SRO mineral–organic complexes that are characteristic of an intermediate (400 ka) weathering stage in basalt-derived soils subjected to a humid climate (Chorover et al., 2004). The A-horizon (6–13 cm) of the *Histic Placic Petraquept* profile was doubled-bagged in a low O_2-permeable, 3-mil Sarenex inner bag and a 4-mil polyethylene outer bag, flushed three times with ultra-pure N_2, packed on ice for transport to the lab and stored at 4 °C. The full depth of the A-horizon was homogenized in a 5% H_2:95% N_2 glove box and stored a 4 °C.

2.3. Initial soil characterization

Total and "labile" element concentrations were measured following Li-metaborate fusion (Hossner, 1996), and 0.5 M HCl (Lovley and Phillips, 1986) and 0.1 M acid ammonium oxalate (AAO) (Loeppert and Inskeep, 1996) extractions. The HCl and AAO extractions were performed at a 1:60 solid to solution mass ratio in 50 mL PPCO centrifuge tubes for 2 h. Tubes were centrifuged for 20 min at 41,500 relative centrifugal force (RCF) and the supernatant solutions were then analyzed using inductively coupled plasma-mass spectrometry (Perkin Elmer DRC II ICP-MS). An initial pH measurement was made on a saturated soil paste (1:1 soil:solution mass ratio in 18 MΩ water). To-

tal soil carbon was analyzed on a Shimadzu 5000A TOC analyzer equipped with a Shimadzu 5000A-SSM solid sample module. Bulk mineral composition was assessed using X-ray diffraction (XRD) on a Philips X'pert MPD diffractometer equipped with a spinning stage and X'Celerator multiple strip detector with Ni-filtered Cu Kα radiation at 50 kV and 40 mA. Quantitative analysis of Fe solids was achieved using Mössbauer spectroscopy as described in Section 2.7.

2.4. Redox reactor design

A redox-stat reactor system was designed and constructed to control the E_h and pH of soil suspensions (Fig. 1). The design is based on a modification of those reported in Patrick et al. (1973) and Petrie et al. (1998). The lower section of the Pyrex glass reactor contains a working volume of 600 mL and a water jacket for precise temperature control. The upper section contains six Ace glass thread connectors for probes and sampling. Redox conditions are controlled by automated modulation of air and N_2 gas flow to maintain set E_h values using three ORP controllers (Oakton Instruments, Vernon Hills, IL, USA). A constant stream of ultra-pure N_2 gas is delivered to the reactors through a 4 M NaOH CO_2 trap/humidifier. Careful attention was paid to the design of the gas handling system (using a series of regulators and flow meters) to ensure that each reactor would receive additions of air and N_2 based on reactor-specific E_h measurements, without influencing the operation of the other replicate reactors. The effluent gas from each reactor was routed through a series of vessels containing base (1 M NaOH) to trap evolved CO_2 (Zibilske, 1994; Majcher et al., 2000). The CO_2 evolution results will be discussed in a forthcoming paper.

2.5. Redox oscillation experiment

2.5.1. Reactor operation

Soil suspension incubations were conducted in the absence of light using field moist soil at a solid (dry mass equivalent) to solution mass ratio of approximately 1:11. Field moist soil was transferred from 4 °C storage to the glove box where it was suspended in 0.02 mM NaCl background electrolyte solution (prepared from deoxygenated 18.2 MΩ water) in a 2 L polyethylene (PE) bottle. The suspension was shaken for 5 min and then the passed through a 1-mm sieve to remove large rocks and particles. This procedure was repeated several times until an uniform slurry was obtained. The slurry was then sealed in the PE bottle and removed from the glove box. The slurry was shaken just prior to transferring 500 mL to each of the reactors in the order A, B and C. The mass of slurry added was recorded, the reactors were sealed, and a stream of N_2 gas was introduced to start the experiment, which was conducted at 25 °C. The precise solid concentration was determined at each sampling point by oven-drying (110 °C) a measured mass of the slurry for 24 h.

Several constraints were applied to isolate the cumulative effects of multiple redox cycles. (1) A full oscillation consisted of 7 d of Fe reducing conditions followed by 7 d of Fe oxidizing conditions. (2) On the second day of each oxidizing half-cycle the pH was reset to 4.5 using 4 M NaOH or 0.5 M HCl. This was necessary to curtail the acidifying effects of organic acid accumulation that

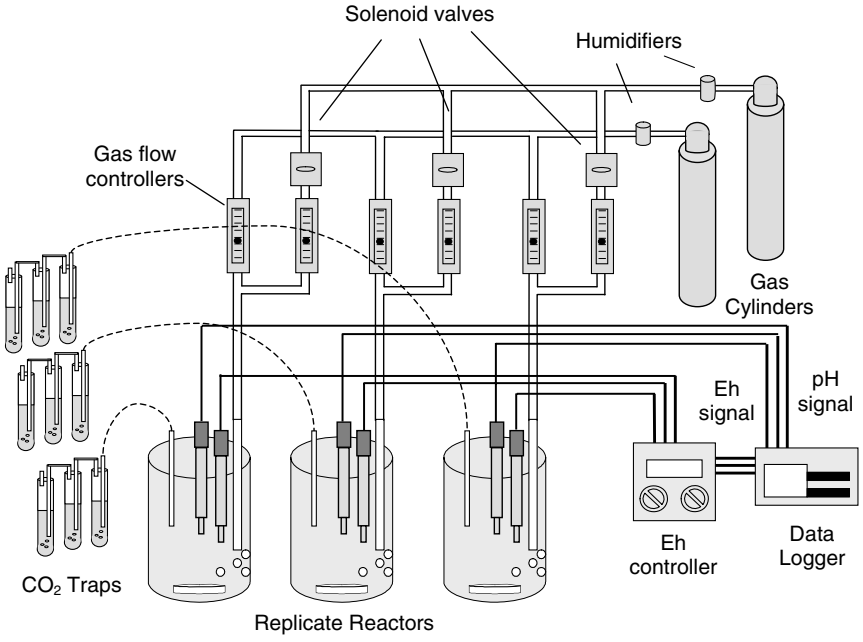

Fig. 1. Schematic of the Fe redox oscillation reactors.

affected Fe transformation rates over time in preliminary experiments. (3) The rate of $O_{2(g)}$ addition during the oxidizing half-cycles was controlled by setting a target E_h to give $Fe^{II}_{(aq)}$ concentrations of 1 μM in equilibrium with "soil Fe" ($Fe(OH)_3$, assuming $K_{diss} = 15.74$) (Lindsay, 1979). This required adjusting the E_h set-point as the pH changed during the oxidizing half-cycle. (4) A supplemental C source (sucrose) was provided at the beginning of each reducing half-cycle (excluding the first half-cycle) to provide consistent initial aqueous C concentrations of 100 mg L^{-1}. All reactors were operated for 8 weeks except reactor C, which malfunctioned in the middle of week 7.

2.5.2. Reactor sampling scheme

The reactors were sampled on days 1, 4, and 7 of each half-cycle. The sampling scheme included taking two 1-mL samples for centrifugal separation of dissolved suspension constituents to <30 nm followed by ultra-filtration to <3 kDa of one of the samples. An additional 1 mL sample was collected for immediate tracking of Fe^{II} and DOM concentrations (<30 nm). Two 1.5 mL samples were collected for archival purposes and one 0.5 mL sample was collected for dry weight analysis. All sample vials were flushed with N_2 gas immediately before and after adding the sample. Each sealed sample was transferred to the 95:5% N_2:H_2 glove box, opened and allowed to equilibrate for 5 min before resealing. After this point samples were opened only inside the glove box.

Samples for dissolved constituents were removed from the glove box and separated by centrifugation in an Eppendorf 5417C centrifuge with an F 45-30-11 rotor. Centrifugal fractionation was accomplished assuming spherical particle geometry and a nominal particle density of 2.72 g cm^{-3} for dispersed particles; the RCF and time required to achieve separation of particles <30 nm (30 min at ~18 k RCF) was calculated from Stokes' law. The mean particle density estimation is based on preliminary elemental analysis of soil colloids. Samples were returned to the glove box where the supernatant solutions were removed and acidified to pH 1 with trace metal grade 6 M HCl (0.8% of sample volume; To et al., 1999). One of the supernatant solutions from the centrifuged samples was passed through a 3 kDa molecular weight cutoff (MWCO) Millipore Amicon-Microcon YM-3 regenerated cellulose filter using an Eppendorf Minispin Plus centrifuge. Since the YM-3 filter apparatus did not seal tight enough to exclude O_2, ultrafiltration was conducted inside the glove box.

The pellets were resuspended in 0.5 M HCl and extracted for 2 h at 7 rpm on an end-over-end rotator. This extraction targets the most soluble short-range-ordered (SRO) Fe oxides (Kostka and Luther, 1994) and releases any ferrous (Fe^{2+}) bound to particle surfaces (Lovley and Phillips, 1986). The samples were centrifuged at 18 k RCF for 5 min, returned to the glove box for aspiration of the supernatant solution, and the resulting pellet was resuspended in a 0.2 M AAO solution with a final pH of 3 (the pH of the AAO stock solution was adjusted to compensate for the entrained 0.5 M HCl in the pellet) for 2 h on a 7-rpm rotator. Samples were then centrifuged at 18 k RCF for 5 min, returned to the glove box, the supernatant solution was removed and the resulting pellet was frozen. All collected solutions were stored at 4 °C until analysis. Archival samples were frozen immediately after equilibration in the glove box.

2.6. Chemical analysis

Redox-stat reactor pH and E_h voltages were logged continuously using a custom designed voltage amplifier/processor that fed a signal to a data logger (B&B Electronics, Ottawa, IL). Gel-filled pH (VWR scientific products) and E_h (Omega, Stamford, CT) electrodes were used because of their low electrolyte leak rates. All suspension solutions and HCl extracts were prepared similarly for analysis of Fe^{II} using the ferrozine method (Stookey, 1970) by UV–Vis spectrophotometer (Shimadzu UV-3101 PC). Interferences in the measurement of Fe^{II} from colloidal material or Fe^{III}–ferrozine complexes (To et al., 1999; Viollier et al., 2000; Washington et al., 2004) were identified by calculating the ratio of absorbance at 562 and 500 nm (A_{562}/A_{500}), which is ca. 1.9 for a pure ferrozine–Fe^{II} complex, but decreases with increasing interference. Solutions yielding $A_{562}/A_{500} < 1.8$ were acidified (after the ferrozine–Fe^{II} complex had formed at neutral pH) to pH 1.5 by addition of a small volume of 6 M HCl. This acidification diminishes interferences but does not destroy the ferrozine–Fe^{II} complex (To et al., 1999). The samples were then centrifuged at 10 k RCF for 5 min, and re-analyzed. A set of standards was also subjected to this acidification step. This restored the A_{562}/A_{500} ratio to >1.8, yielding a lower and more accurate Fe^{II} reading. Total metal concentrations (Fe, Si, Al, Ti, K, Mg, Ca, and Na) were measured via ICP-MS. Dissolved organic carbon (DOC) measurements used to define sucrose additions were achieved by high temperature combustion and subsequent infrared detection of CO_2 on a Shimadzu 5000A TOC analyzer.

2.7. Mössbauer spectroscopy

Solid phase Fe mineralogical changes were assessed using room temperature (RT, 22 °C) and liquid helium temperature (LHeT, 4.2 K) ^{57}Fe Mössbauer spectroscopy (MBS). Three freeze-dried splits of the reactor soil material were analyzed: (1) sample V3, native soil, frozen at −80 °C immediately after the homogenation process (see Section 2.2). (2) sample 1A, archived slurry (frozen immediately after sampling) from the first sampling point (day 1) and (3) sample 8C, archived slurry (frozen immediately after sampling) from the last sampling point (day 56) of reactor B in the redox oscillation experiment.

All LHeT and RT ^{57}Fe Mössbauer spectra were collected in transmission mode using a 10–50 mCi ^{57}Co–Rh source kept at RT. Freeze-dried powder samples were

mounted in holders with 1.27-cm diameter windows and a thickness as large as 0.64 cm to accommodate large volumes of sample. In all cases, an amount of sample corresponding to the calculated ideal absorber thickness that optimizes the signal to noise ratio (Rancourt et al., 1993) was used (~100 mg per holder). The ideal thickness is calculated on the basis of the bulk elemental composition of the dry powder and, with OM-rich samples, can require as much as 500 mg or more of sample. With heterogeneous samples such as the Hawaiian soils (<15% dry mass Fe), it is essential to use the ideal absorber thickness, especially with cryogenic measurements where the data collection time is limited (by labor and cryogen costs) to approximately 1 d. The RT measurements had data accumulation times of 1–2 wk.

All measurements were performed with a velocity range of ± 11 mm s^{-1} to ensure detection of any hyperfine split patterns (i.e., sextets) from Fe^{III}-bearing magnetically ordered phases (esp., oxides and oxyhydroxides). All Fe-bearing solid phases, including sorbed species, were detected down to the typical detection limit of 0.1–1% of Fe (or worse for some subspectral patterns and the smaller signal/noise ratio spectra). Velocity (i.e., γ-ray energy) calibration was obtained using an enriched ^{57}Fe foil at RT and all center shifts (CSs) and peak positions are reported with respect to the CS of metallic iron at RT. The transducer was operated in constant acceleration mode and folding was performed to achieve a flat background. The spectra were not corrected for thickness effects (Rancourt et al., 1993). The cryogenic measurements were performed in a He gas flow type cryostat with cryogenic radiation shielding. Temperature was monitored both at the He gas outflow port and on the sample holder mount and did not rise above 4.5 K at any time during data accumulation. This method is known not to produce measurable temperature gradients across the absorber dimensions (less than 0.1 K on 1/2 in.). The entire setup is vibration isolated and tests showed no measurable vibrational broadening on calibration standard peaks (less than 0.001 mm/s on peak widths).

Mössbauer spectral fitting of all the RT and LHeT spectra was performed using the Voigt-based fitting (VBF) method of Rancourt and Ping (1991) for quadrupole splitting distributions (QSDs) and combined hyperfine field distributions (HFDs), as implemented in the Recoil software, developed in Rancourt's laboratory in collaboration with ISA Inc. (http://www.isapps.ca/recoil). All VBF Mössbauer parameter definitions and a description of the relevant notation are given by Rancourt and Ping (1991). All errors in Mössbauer fitting parameters are two-SD (2σ) errors, as calculated by Recoil. In reporting quantitative phase abundances or site populations it is assumed that the Mössbauer recoilless fractions of all detected phases or Fe-bearing components are equal, such that subspectral areas (expressed as fractions of total spectral area) are equal to the amounts of Fe (expressed as fractions of total Fe) in the corresponding phases or components. This assumption is expected to be valid at cryogenic temperatures, and also to be a good approximation at RT with dry samples (Lalonde et al., 1998; Rancourt, 1998).

2.8. Calculations

All aqueous and solid phase concentration values are expressed in units of moles per kilogram of dry soil to compensate for small variations in suspension solid concentration. During the reactor experiment, some soil particles were deposited onto the upper portion of the reactor vessel, effectively removing them from the bulk suspension and resulting in a minor (<4%) increase in the suspension water content over the course of the experiment. Suspension dry mass was determined each time a sample was taken. Concentrations of analyte in the HCl and AAO extracts were determined after correcting for their concentrations in the entrained solution prior to extractant addition:

$$[\mathrm{Fe}]_{\mathrm{HCl}} = \frac{\left[[\mathrm{Fe}]^{\mathrm{S}}_{\mathrm{HCl}} \cdot M_{\mathrm{HCl\ sol'n}} - [\mathrm{Fe}]^{\mathrm{S}}_{<30\ \mathrm{nm}} \cdot M^{<30\ \mathrm{nm}}_{\mathrm{Entr'n\ sol'n}}\right]}{M_{\mathrm{Soil}}}, \quad (1)$$

$$[\mathrm{Fe}]_{\mathrm{AAO}} = \frac{\left[[\mathrm{Fe}]^{\mathrm{S}}_{\mathrm{AAO}} \cdot M_{\mathrm{AAO\ sol'n}} - [\mathrm{Fe}]^{\mathrm{S}}_{\mathrm{HCl}} \cdot M^{\mathrm{HCl}}_{\mathrm{Entr'n\ sol'n}}\right]}{M_{\mathrm{Soil}}}, \quad (2)$$

where $[Fe]^{S}_{<30\ nm}$, $[Fe]^{S}_{HCl}$, and $[Fe]^{S}_{AAO}$ refer to the concentration of Fe (mmol kg^{-1} sol'n) in the <30 nm fraction, HCl and AAO solutions, respectively. $M_{HCl\ sol'n}$ and $M_{AAO\ sol'n}$ refer to the mass (kg) of HCl and AAO solution, respectively. $M^{<30\ nm}_{Entr'n\ sol'n}$ and $M^{HCl}_{Entr'n\ sol'n}$ refer to the mass of entrained solution in the HCl and AAO extraction, respectively. Concentration values (e.g., $[Fe]_{HCl}$) have been corrected for Fe mass in entrained solutions from the preceding step. The sum of the aqueous, HCl and AAO concentrations approximates the standard AAO extraction (Kostka and Luther, 1994; Loeppert and Inskeep, 1996) and is defined as:

$$[\mathrm{Fe}]_{\mathrm{SRO}} = [\mathrm{Fe}]_{<30\ \mathrm{nm}} + [\mathrm{Fe}]_{\mathrm{HCl}} + [\mathrm{Fe}]_{\mathrm{AAO}} \quad (3)$$

Ionic strength (I) was calculated for each sampling point from measured values of the major cations assuming Cl^- balances the cation charge. Fe^{2+} activity was then calculated using the Davies equation.

3. Results

3.1. Initial soil characterization

Selected physical–chemical characteristics of the soil used in these experiments are presented in Table 1. The mineral composition of the soil is dominated by SRO Fe (primarily nano and microcrystalline goethite) and Al oxides. Strong XRD patterns were observed for quartz and anatase, along with weak patterns for other minor constit-

Table 1
Selected physical–chemical characteristics of the soil

Soil classification	Histic Placic Petraquept		
MAT[a]	16 °C (6–13 cm)		
MAP[a]	3500 mm yr^{-1}		
Horizon	Ag		
Mineralogy[b]	Major: quartz, SRO Fe and Al/Si-oxides (e.g., nano-goethite and allophane). Minor: anatase, muscovite, hematite, ilmenite, and kaolinite		
pH_{oxic} (1:1 soil:H_2O)	4.3		
	Total soil	HCl-extract	AAO-extract
Major element chemistry (g kg^{-1} dry soil)			
Si	130(10)[c]	0.200(5)	0.200(3)
Fe	111(15)	12.6(2)	42.0(24)
Ti	79.3(68)	0.40(6)	7.4(9)
Al	44.1(29)	3.7(11)	5.9(3)
C	107(4)	n.d.[d]	n.d.

[a] Mean annual temperature and precipitation (Schuur and Matson, 2001).
[b] As determined by XRD and Mössbauer analysis.
[c] Values in parenthesis are 95% confidence interval: 95% C.I. = $t \times (SD)/(n^{0.5})$ presented in scientific notation (e.g., 5.0(15) = 5.0 ± 1.5).
[d] Not measured.

uents. The relative elemental composition (oxygen free) of the soil follows the order: Si > Fe > C > Ti > Al.

3.2. Iron dynamics

Reducing half-cycles were characterized by a decrease in E_h, and increases in both pH and Fe^{II} concentration, whereas the oxidizing half-cycles exhibited inverse trends (Fig. 2). $[Fe^{II}]_{<3\ kDa}$ (hereafter also termed "aqueous" Fe^{II}) showed comparable trends between all replicate reactors (Fig. 2C). Measured $[Fe^{II}]_{<3\ kDa}$ values indicated aqueous phase undersaturation with respect to "Soil-Fe" $[Fe(OH)_3]$ during reducing half-cycles and oversaturation during oxidizing half-cycles (Fig. 2C).

Values of $[Fe^{II}]_{HCl}$ showed similar fluctuations (illustrated by $[Fe^{II}]_{<30\ nm\ +\ HCl}$ in order to facilitate discussion below; Fig. 3) to the $[Fe^{II}]_{<3\ kDa}$ data, but at higher concentration. The Fe^{II} distribution coefficient (Kd) for $[Fe^{II}]_{HCl}$ and $[Fe^{II}]_{<3\ kDa}$ fluctuates inversely to $[Fe^{II}]$ (Fig. 4); fractional removal of Fe^{II} from solution exceeds that removed from the solid phase during oxidizing half-cycles. $[Fe^{III}]_{<3\ kDa}$ was never detected—indicating that soluble Fe^{III}–organic complexes are insignificant in these systems—but considerable $[Fe^{III}]_{HCl}$ was present (Fig. 3), with maxima occurring during the oxidizing half-cycles. The net effect of inverse oscillatory behavior in $[Fe^{III}]_{HCl}$ and $[Fe^{II}]_{HCl}$ resulted in $[Fe^{T}]_{HCl}$ maximums ($[Fe^{T}]_{HCl} = [Fe^{III}]_{HCl} + [Fe^{II}]_{HCl}$) at the end of each reducing half-cycle and an overall decrease in $[Fe^{T}]_{HCl}$ with time (Fig. 5). Fluctuations in $[Fe^{T}]_{AAO}$ were of similar relative amplitude to those in $[Fe^{T}]_{HCl}$ (data not shown) with peak values always occurring during the reducing half-cycles. Summing $[Fe^{T}]_{<30\ nm}$, $[Fe^{T}]_{HCl}$, and $[Fe^{T}]_{AAO}$ provides a close approximation to the one-step AAO extraction often used as a proxy for SRO materials, termed $[Fe]_{SRO}$ (Eq. (3); Fig. 5) (Kostka and Luther, 1994; Miller et al., 2001). Note that $[Fe^{T}]_{<30\ nm}$ is used instead of $[Fe^{T}]_{<3\ kDa}$ because these selective chemical extractions were performed on pellets resulting from the targeted <30 nm centrifugations. $[Fe]_{SRO}$ peaked on the last day of each reducing half-cycle, and exhibited a general decline over the course of the experiment.

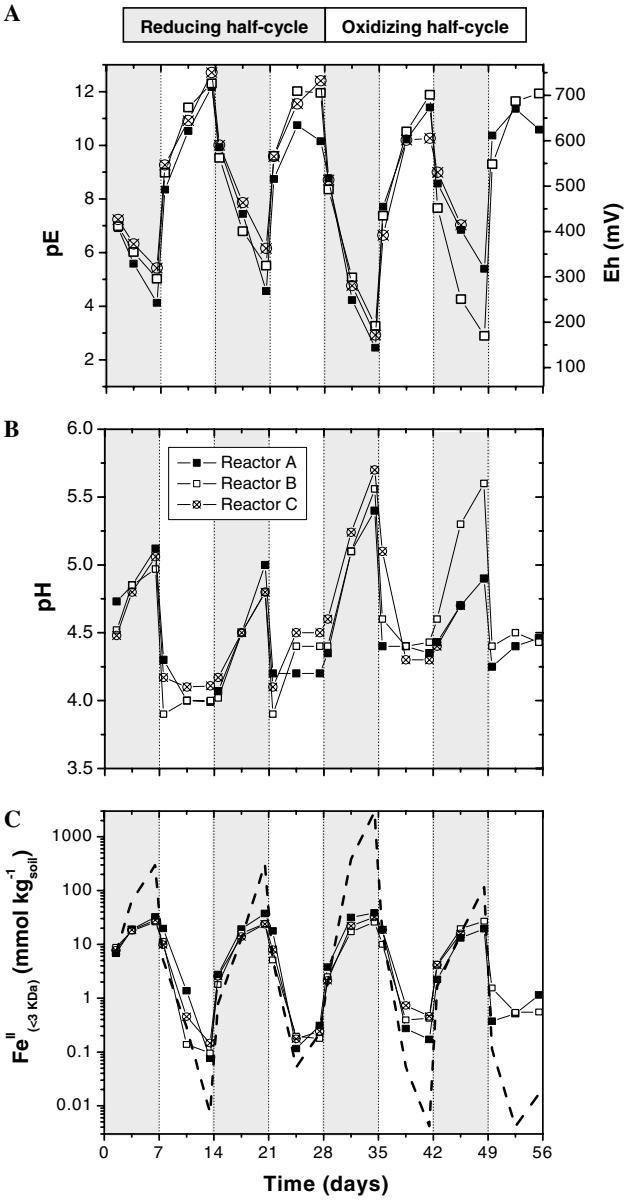

Fig. 2. (A) pE (E_h) and (B) pH data at the time of sampling for all reactors. (C) $[Fe^{II}]_{<3\ kDa}$ for all reactors normalized to the sample solid concentration in the reactor. The dashed line corresponds to the equilibrium Fe^{2+} activity for "Soil-Fe" $[Fe(OH)_3]$ (Lindsay, 1979) at the pH and E_h values shown for reactor A.

The sum of aqueous and HCl extractable Fe^{II} is often used to quantify the total Fe^{II} released during Fe reduction (e.g. Lovley and Phillips, 1986). The amount of aqueous and sorbed Fe^{II} present in the reactor was determined by summing $[Fe^{II}]_{<30\ nm}$ and $[Fe^{II}]_{HCl}$ (Fig. 3). Rates of Fe reduction and oxidation based on this summation averaged

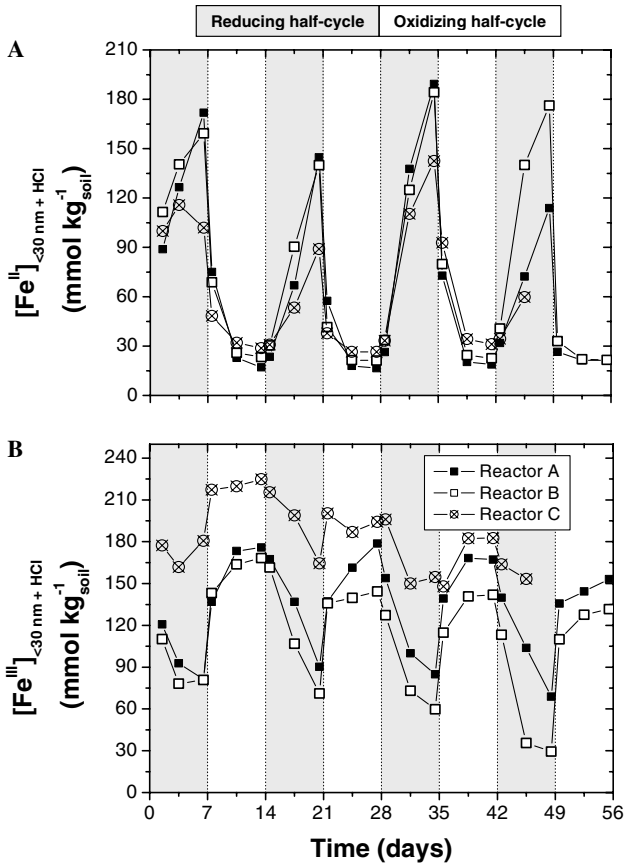

Fig. 3. (A) $[Fe^{II}]_{<30\ nm\ +\ 0.5\ M\ HCl}$ and (B) $[Fe^{III}]_{<30\ nm\ +\ 0.5\ M\ HCl}$ for all reactors normalized to the solid concentration in the reactor. Note that $[Fe]_{<30\ nm}$ is used instead of $[Fe]_{<3\ kDa}$ because the selective chemical extractions were performed on pellets resulting from the targeted <30 nm centrifugations. This summation is the closest approximation to a single HCl extraction of the intact soil suspension.

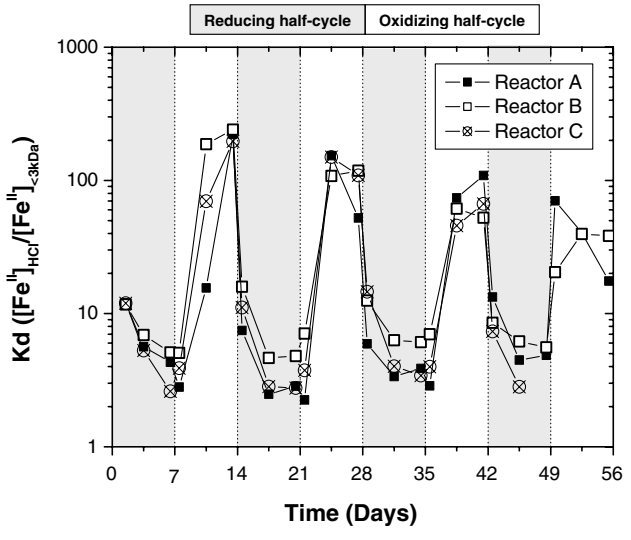

Fig. 4. Partition coefficient $K_d = [Fe^{II}]_{0.5\ M\ HCl}/[Fe^{II}]_{<3\ kDa}$ of Fe^{II} between the aqueous and HCl extractable phases.

ca. 25 and 80 mmol kg_{soil}^{-1} d^{-1}, respectively. These rates did not show any discernable intra-cycle or cumulative trends over the course of the experiment (Fig. 6).

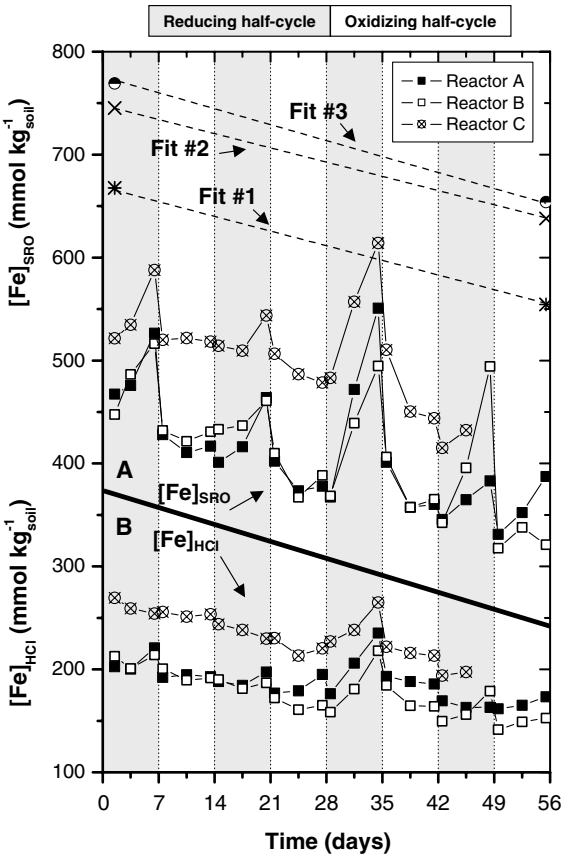

Fig. 5. (A) Sum of $[Fe]_{AAO}$, $[Fe]_{HCl}$ and $[Fe]_{<30\ nm}$ for all reactors normalized to the reactor solid concentration. Note that $[Fe]_{<30\ nm}$ is used instead of $[Fe]_{<3\ kDa}$ because the selective chemical extractions were performed on pellets resulting from the targeted <30 nm centrifugations. This summation is the closest approximation to a single AAO extraction of the intact soil slurry (e.g. Loeppert and Inskeep, 1996). (B) $[Fe]_{HCl}$ for all reactors normalized suspension solid concentration. The symbol and dashed dotted lines above the reactor data points are estimates of the concentration of the nGt component in sample 1A and 8C (reactor B) by ^{57}Fe Mössbauer using the three fitting methods shown in Table 3. Note the similar slopes of the ^{57}Fe Mössbauer and $[Fe]_{SRO}$ data.

3.3. ^{57}Fe Mössbauer characterization

At each collection temperature (RT or LHeT), samples V3 (native soil) and 1A (day 1 of the redox experiment) produced almost identical Mössbauer spectra. Conversely, small but significant changes were detected in sample 8C relative to 1A and V3; all spectra at a given collection temperature contain the same spectral components, but the amounts differ. In Mössbauer spectroscopy, each spectral component corresponds to one Fe-bearing solid phase (or mineral, if crystalline) or to a group of unresolved Fe-bearing solid phases. In addition, assuming equal Mössbauer recoilless fractions (Rancourt, 1998), the total spectral area of a given component is proportional to the amount of Fe in the corresponding solid phase(s).

3.3.1. Soil Fe mineral composition

In the RT spectra, five spectral components were resolved (Fig. 7): (1) an Fe^{III} quadrupole doublet (labeled Q)

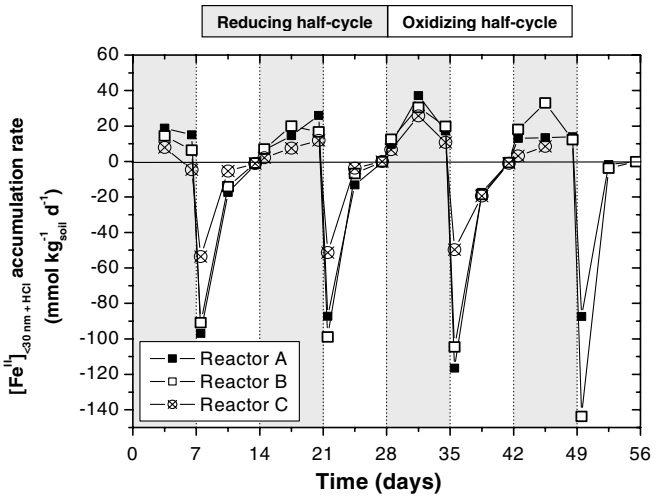

Fig. 6. Fe reduction (positive values) and Fe oxidation (negative values) rates for all reactors. Rates were calculated from $[Fe^{II}]_{<30\ nm\ +\ HCl}$ normalized to reactor solid concentration. Values for the previous sampling point (e.g. day 1) were subtracted from the current sampling point (e.g., day 4) and then divided by the number of days separating them (e.g., 3 days).

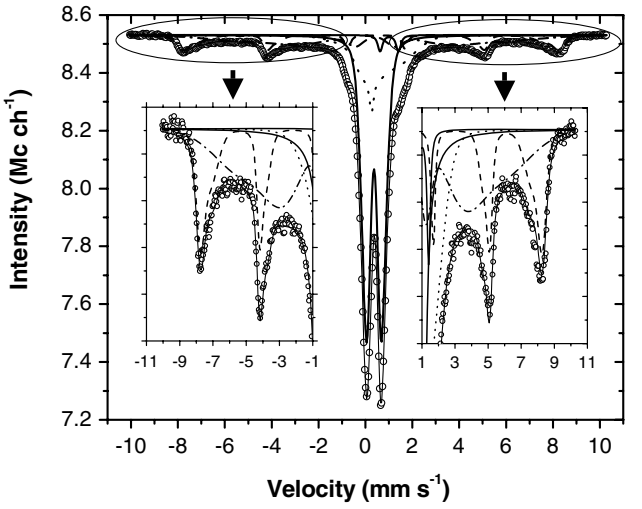

Fig. 7. Fitted RT ^{57}Fe Mössbauer spectrum of the native soil (sample V3). Fit III-*z* (see Table A1) is shown. The high and low velocity wings of the spectrum are also shown on an expanded vertical scale to better visualize the sextet components. The thin solid line is the total calculated fit, through the discrete data points. The five resolved spectral components described in the text are: (1) Q, the dominant doublet with lines at +0.02 and +0.72 mm/s (solid line); (2) Il, a minor doublet with lines at +0.63 and +1.41 mm/s (solid line); (3) mc-Hm, a relatively sharp sextet with asymmetric peaks (dashed line); (4) mc-Gt, a highly broadened sextet (dotted line); and (5) b-Gt, a highly broadened (collapsed sextet) central contribution (dash-dotted line).

corresponding to Fe^{III} in silicates, surface-complexed to solids, and in all Fe oxyhydroxides that are superparamagnetic (SP) at RT; (2) a low-spin Fe^{II} quadrupole doublet (labeled Il) that is attributed to ilmenite ($FeTiO_3$); (3) an Fe^{III} sextet (labeled mc-Hm) corresponding to micro-crystalline hematite; (4) a broadened Fe^{III} sextet (labeled mc-Gt) attributed to micro-crystalline goethite; and (5) a partially collapsed Fe^{III} 'sextet' (labeled b-Gt) that must be due to a non-ferrihydrite-like Fe oxyhydroxide having its SP blocking temperature near RT and that is attributed to blocking-transition ('RT-blocked') goethite.

In the LHeT spectra, four spectral components were resolved (Fig. 8): (1) an Fe^{III} quadrupole doublet (labeled Q′) corresponding to Fe^{III} in non-Fe-rich silicates and complexed to solids such as OM; (2) a mc-Hm component that has the same spectral area, within error, as the RT mc-Hm component; (3) a goethite (Gt) component, that has a spectral area equal to the sum of the spectral areas of the mc-Gt and b-Gt components of the RT spectra, and that we label mc + b-Gt; and (4) a partially collapsed Fe^{III} 'sextet' (labeled n-Gt) that is attributed to Fe oxyhydroxides having their SP blocking temperatures near LHeT ('LHeT-blocked').

Taken together, the RT and LHeT spectra of the native soil (Figs. 7, 8 and Appendix A) reveal a quantitative Fe solid phase composition dominated by nano- and microcrystalline goethite, that includes significant micro-crystalline hematite, no ferrihydrite, and only a small amount of Fe^{II} present as ilmenite (Table 2). All the fitting parameters are given in Appendix A (three different fitting models were used for the RT spectra, see Section 3.3.2).

Assignment of the components in Table 2 are based on synthesis of the RT and LHeT spectral interpretations and by the known Mössbauer behaviors of the phases involved. Quantitative assignments are based on Fit III-*z* of the RT spectra (see Table A1) and are corroborated by information obtained at LHeT (i.e., the separation of Q′ from Q). Justification of each of the component assignments in Table 2 follows: (Il) The ilmenite doublet gives rise to a characteristic RT peak at 1.4 mm/s. Only epidote could

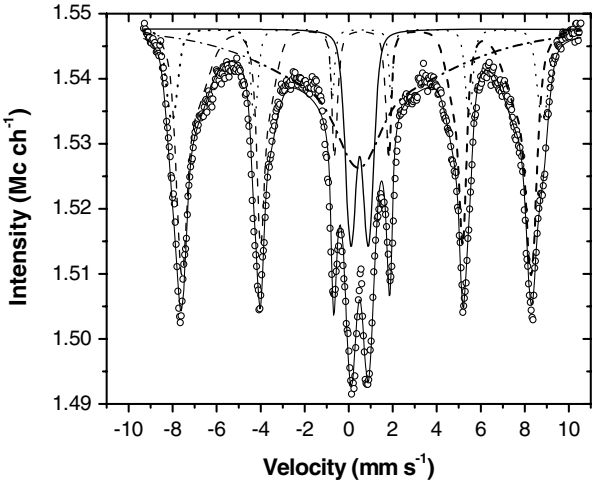

Fig. 8. Fitted (fit-n, see Table A2) LHeT ^{57}Fe Mössbauer spectrum of the native soil (sample V3). The thin solid line is the total calculated fit, through the discrete data points. The four resolved spectral components described in the text are: (1) Q′, a doublet giving rise to the two deepest central peaks (solid line); (2) mc-Hm, a relatively small sextet having the outermost peaks (dashed line); (3) mc + b-Gt, corresponding to the dominant (i.e., deepest peaks) sextet (dotted line); and (4) n-Gt, a largely collapsed 'sextet' (dash-dotted line). The minor Il component seen at RT is not detected in the lower signal/noise ratio LHeT spectra.

Table 2
Quantitative Fe mineralogy from Mössbauer analysis

Component ID	Component description	% of total Fe
n-Gt	Nano-goethite (SP at RT, LHeT-blocked)	39.0(10)[a]
mc + b-Gt	Micro-crystalline and RT-blocked Gt	37.0(10)
Q′	Fe^{3+} surface-complexed and in silicates	12.5(8)
mc-Hm	Micro-crystalline hematite	10.5(6)
Il	Ilmenite	1.7(1)

[a] Values in parentheses are two-SD non-linear least squares fitting errors, calculated by the gradient at the minimum method. All errors are in scientific notation (e.g., 5.0(15) = 5.0 ± 1.5).

also have such a peak but its low energy doublet component would be detected and it is not. An Il component is not resolved at LHeT because of spectral overlaps and smaller signal/noise. No high-spin Fe^{II} components were detected in any of the spectra, with a RT detection limit of ca. 0.2% of total-Fe. (mc + b-Gt) This component is clearly resolved as goethite at LHeT and can be further divided approximately equally (50 ± 10%) into mc-Gt and b-Gt in the RT spectra (see Appendix A). (mc-Hm) The RT mc-Hm component has hyperfine parameters corresponding to micro-crystalline hematite (on the protohematite–hydrohematite join) with crystallite diameters ~100 nm (Dang et al., 1998). This is confirmed by the fact that the mc-Hm component at LHeT has hyperfine parameters corresponding to samples that have not undergone the Morin transition (Dang et al., 1998). (Q′) This component is directly resolved in the LHeT spectra and contributes to the Q component at RT. Unlike the Q component of RT spectra, the Q′ component of LHeT spectra cannot contain any contribution from Fe oxyhydroxides since all known Fe oxyhydroxides are blocked (i.e., are not SP) at 4.2 K. (n-Gt) Natural nano-goethites (n-Gt) are SP at RT (Van Der Zee et al., 2003), as are all ferrihydrite-like (Fh-like) natural and synthetic Fe oxyhydroxides. The n-Gt component has been predominantly assigned to nano-goethite, as it has a similar behavior to the n-Gt components seen in lake and marine sediments (Van Der Zee et al., 2003) and since the only other candidate, ferrihydrite-like coprecipitates, generally have much more developed sextet features. If ferrihydrite is present, it is likely very minor as only goethite-like particles are expected to have sufficiently small blocking energies to have blocking temperatures near LHeT. All of the synthetic and natural Fh-like precipitates studied in Rancourt's laboratory (Van Der Zee et al., 2003; supplementary material, unpublished) have more developed LHeT sextet features than the n-Gt component. Note that the n-Gt component can be calculated either directly from the n-Gt component resolved at LHeT or as Q–Q′, since this phase is SP at RT.

3.3.2. Changes in Fe mineral composition resulting from redox oscillations

Quantitative Mössbauer results, corresponding to the fits described in Appendix A, are given in Tables 3 and 4. Since relatively small changes in *bulk* Fe mineral composition occur on redox cycling (redistributions of Fe of ca. 5% of total-Fe) it is important to examine the possible systematic errors that can occur on fitting the Mössbauer spectra. The spectral characteristics of the resolved components allow reliable identification of the corresponding Fe-bearing solid phases, within the limits described above. The only

Table 3
Quantitative[a] Fe-bearing solid phase results from RT Mössbauer spectra

Sample	Fit[e]	Q	mc-Hm	mc-Gt	b-Gt	mc-Gt + b-Gt	Ilmenite
Series-I fits							
1A	I-q	46.1(7)[b,c]	11.0(7)	14.5(9)	28.4(5)	42.9(7)	n/a
V3	I-h	45.6(5)	9.7(6)	14.9(7)	29.8(4)	44.7(6)	n/a
8C	I-d	40.4(7)	12.4(9)	15.4(10)	31.8(6)	47.2(9)	n/a
(8C-1A)		−5.7(10)[d]	1.4(11)	0.9(13)	3.4(8)	4.3(11)	
Series-II fits							
1A	II-s	50.0(11)	11.3(6)	20.4(9)	15.9(14)	36.3(17)	2.4(2)
V3	II-k	48.3(11)	11.8(6)	20.9(11)	16.6(12)	37.5(16)	2.3(2)
8C	II-g	44.6(11)	14.5(7)	22.9(11)	15.6(13)	38.5(17)	2.4(2)
(8C-1A)		−5.4(16)	3.2(9)	2.5(14)	−0.3(18)	2.2(24)	0.0(3)
Series-III fits							
1A	III-z	51.2(9)	10.5(6)	16.9(9)	19.7(9)	36.6(13)	1.7(1)
V3	III-o	49.6(11)	10.2(6)	18.1(9)	20.8(13)	38.9(16)	1.3(2)
8C	III-L	45.4(16)	13.3(10)	21.9(13)	17.5(20)	39.4(24)	1.8(2)
(8C-1A)		−5.8(18)	2.8(11)	5.0(15)	−2.2(22)	2.8(27)	0.1(2)

[a] All results are expressed as % of total-Fe, assuming equal Mössbauer recoilless fractions.
[b] Errors (in parentheses) are in scientific notation (e.g., 5.0(15) = 5.0 ± 1.5).
[c] All errors are two-SD non-linear least squares fitting errors, calculated by the gradient at the minimum method.
[d] Errors for sums and differences are calculated assuming statistical independence. This is an overestimate for the error in mc-Gt + b-Gt.
[e] The corresponding fits are those given in Table A1.

Table 4
Quantitative[a] Fe-bearing solid phase results from LHeT Mössbauer spectra

Sample	Fit[d]	Q′	mc-Hm	mc + b-Gt	n-Gt
1A	n	12.5(8)[b,c]	11(2)	39(3)	37(2)
V3	ee	12.2(8)	9(2)	46(2)	33(2)
8C	nn	14.1(9)	10(2)	41(2)	35(2)

[a] All results are expressed as % of total-Fe, assuming equal Mössbauer recoilless fractions.
[b] Errors (in parentheses) are in scientific notation (e.g., $5.0(15) = 5.0 \pm 1.5$).
[c] All errors are two-SD non-linear least squares fitting errors, calculated by the gradient at the minimum method.
[d] The corresponding fits are those given in Table A2.

other uncertainties arise from fitting non-uniqueness and fitting tradeoffs (Rancourt, 1998). For these reasons, we concentrate on the higher signal/noise ratio RT spectra and report the results from three different fitting models (I, II, and III, see Table A1). Model-I does not include the small ilmenite doublet but is otherwise identical in its assumptions to model-II. Model-III includes the ilmenite doublet and allows more freedom in describing the spectral shape of the b-Gt component than does model-II. This acknowledges that dynamically broadened spectra corresponding to SP particles near their blocking temperatures can be rather complicated and are not necessarily well represented by static HFDs (Rancourt, 1998).

The fit qualities increase in the sequence I < II < III, with typical reduced chi squared ranges of ca. 5–7, ca. 2–4, and ca. 1.5–2.0, respectively (see Table A1). Despite some systematic differences between fitting model results (Table 3), the decrease in Q component of $-5.8 \pm 0.9\%$ of total-Fe (one-SD error, series-III fits) is robust, as is the corresponding increase in the mc-Hm + mc-Gt + b-Gt component taken as a whole. The LHeT results (Table 4) show the Q′ component not to change significantly on redox cycling, implying that the significant change in the (RT) Q component must be due to a decrease in n-Gt.

3.4. Metal partitioning

Dilute HCl and AAO extractions are designed to dissolve poorly crystalline minerals (Kostka and Luther, 1994). In general the intra-cycle responses of Si, Al, and Ti were attenuated in comparison to Fe, and they showed minor peaks at the end of the reducing half-cycles (Figs. 9 and 10). Similar to the case for Fe, $[Al]_{HCl}$ and $[Al]_{SRO}$ decreased over the course of the experiment (Fig. 10). However, $[Ti]_{HCl}$ was observed to increase with time, whereas little trending was measured for $[Ti]_{SRO}$ (Fig. 9). The sequential extractions (HCl followed by AAO) yielded relatively consistent $[M]_{AAO}$: $[M]_{HCl}$ ratios over the course of the experiment for Fe (1.1 ± 0.1, SD), Al (0.5 ± 0.1), and Si (0.6 ± 0.2); but Ti (15.0 ± 4.6) exhibited a strongly decreasing trend because of the marked increase in $[Ti]_{HCl}$ over the course of the experiment (Fig. 9A). Soluble silica

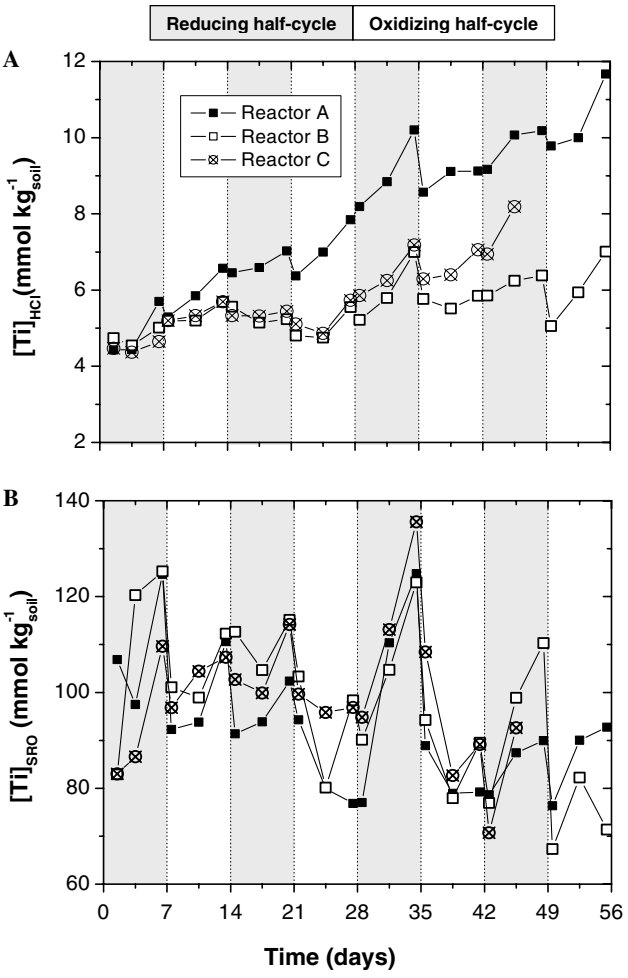

Fig. 9. (A) $[Ti]_{HCl}$ for all reactors normalized suspension solid concentration. (B) Sum of $[Ti]_{AAO}$, $[Ti]_{HCl}$ and $[Ti]_{<30\ nm}$ (e.g., $[Ti]_{SRO}$) for all reactors normalized to the reactor solid concentration. Note that $[Ti]_{<30\ nm}$ is used instead of $[Ti]_{<3\ kDa}$ because the selective chemical extractions were performed on pellets resulting from the targeted <30 nm centrifugations.

($[Si]_{<3\ kDa}$) increased from less than 1 mmol kg^{-1}_{soil} to 16, 15, and 40 mmol kg^{-1}_{soil} (reactors A, B and C, respectively) at the end of the experiment, with only minor increases in $[Si]_{HCl}$ and $[Si]_{SRO}$ (data not shown). This most likely reflects steady state dissolution of soil silicates, although contributions of reactor vessel glass can not be ruled out.

4. Discussion

4.1. Solid phase Fe speciation

Mössbauer analysis of the soil reveals an Fe mineral assemblage that is dominated by goethite (Gt) particles ranging in size from nanometer (ca. 10 nm) to micrometer-scale (100's of nm). The conspicuous absence of ferrihydrite in this soil is intriguing, as rapid weathering of volcanic debris has often been thought to produce considerable ferrihydrite (Parfitt et al., 1988; Shoji et al., 1993), especially at intermediate-aged weathering stages in humid

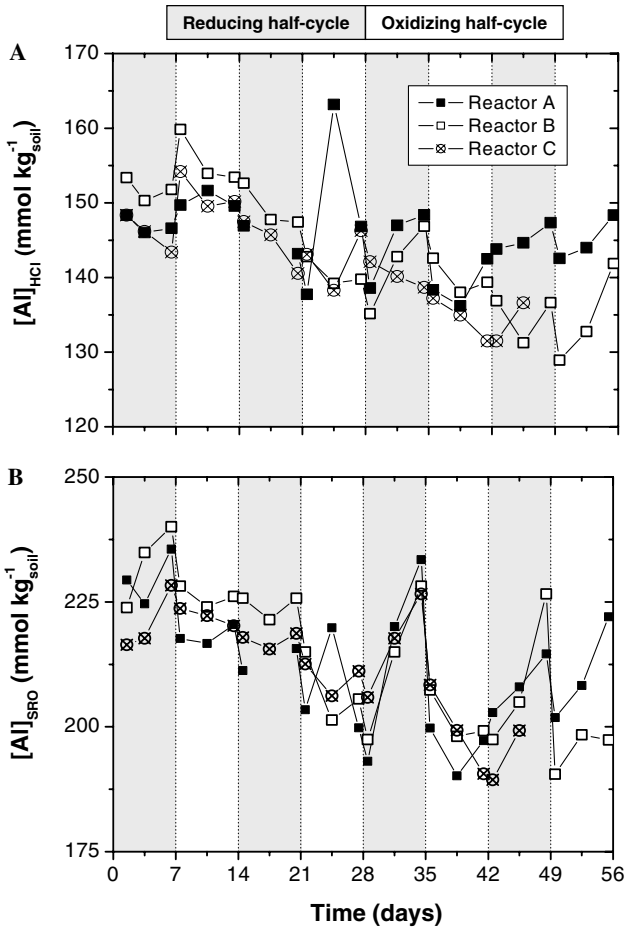

Fig. 10. (A) $[Al]_{HCl}$ for all reactors normalized suspension solid concentration. (B) Sum of $[Al]_{AAO}$, $[Al]_{HCl}$ and $[Al]_{<30\ nm}$ (e.g., $[Al]_{SRO}$) for all reactors normalized to the reactor solid concentration. Note that $[Al]_{<30\ nm}$ is used instead of $[Al]_{<3\ kDa}$ because the selective chemical extractions were performed on pellets resulting from the targeted <30 nm centrifugations.

systems (Chorover et al., 2004). Previous identification of ferrihydrite in similar volcanic soils (e.g. Chorover et al., 2004) was based on non-Fe-specific techniques (e.g., XRD, FTIR, dissolution kinetics) or by using Mössbauer spectroscopy at only 298 and 77 K (Parfitt et al., 1988) and thus, it is plausible that if both RT and LHeT Mössbauer had been used for characterization, what was previously identified as ferrihydrite would be better described as nano-goethite (Van Der Zee et al., 2003). The native soil nano-goethite phase identified by MBS contains a similar magnitude of Fe (ca. 43 g kg^{-1}) as the initial AAO extraction of the soil (42 g kg^{-1}; Table 1), implying that nano-goethite is solubilized by an AAO extraction.

Although the HCl extraction indicated the presence of Fe^{II} at ca. 5 and 1% of total-Fe in samples 1A and 8C, no high-spin (non-ilmenite) Fe^{II} is detected in the Mössbauer spectra. Oxidation of Fe^{II} during freeze drying has been reported (Murad and Cashion, 2004), but it is generally assumed to be negligible if anoxic procedures are followed carefully (Murad and Cashion, 2004), as they were in the present study. If the $[Fe^{II}]_{HCl}$ was indeed oxidized during the freeze drying process, that would explain the lack of high-spin ferrous in the RT Mössbauer spectra. To test this hypothesis, quadruplicate samples of the reactor slurry were split into two groups in a 5% H_2:95% N_2 glove box, one group was extracted with 0.5 M HCl and the other group was frozen, freeze-dried in accordance to methods used for Mössbauer analysis, and then extracted with 0.5 M HCl. Freeze drying led to a 41 ± 7% (95% Confidence Interval) reduction in the recovery of $[Fe^{II}]_{HCl}$, relative to the wet slurry (data not shown), which implies that sample 1A would still contain ca. 3% of the total-Fe as $[Fe^{II}]_{HCl}$. Assuming equal recoilless fractions in the RT MBS, the limit of detection is ca. 0.2% of total-Fe. It is possible that Fe(II) complexed to dry OM (the most likely form of $[Fe^{II}]_{HCl}$ after freeze-drying) may have a significantly smaller RT recoilless fraction than Fe in mineral solids; RT recoilless fraction determinations of Fe sorbed to dry OM have not been determined previously. In LHeT-MBS, where all recoilless fractions must be equal, the signal/noise of the spectra are not as good as at RT. Therefore, a high spin ferrous doublet as large as 3% of total Fe could be present, but such a doublet is not obviously needed (i.e., not statistically required in that many other features of the resulting residual would be as large as the ferrous peak that one could include). The quantitative results of Table 2 are based on RT only, where non-ilmenite ferrous is not detected. This non-detection can only mean either: (1) high-spin ferrous does not exist in the sample or (2) it has an anomalously small recoilless fraction relative to all other Fe-bearing phases detected (or some combination within the 0.2% limit). If reason (2) is correct, then all the conclusions of Table 2 are nonetheless correct except that one must interpret "total-Fe" to mean "total-detected-Fe" (i.e., having a normal recoilless fraction).

4.2. Iron redox cycles as a biogeochemical forcing function

Fe redox cycles were used as a sinusoidal forcing function to perturb the biogeochemistry of the soil suspension. The use of a sinusoidal forcing function, comprising a constant frequency of oscillation, contrasts with the step or pulse forcing more commonly used (Gotoh and Patrick, 1974; Patrick and Henderson, 1981; Quantin et al., 2001; Zachara et al., 2001) to study biogeochemical parameters (i.e., a single change in redox status from oxic to anoxic or vice versa). Repeating sets of two week cycles comprising a 7 d reduction period followed by 7 d of oxidation were employed to represent temporally dynamic redox conditions in humid forest soil environments (Silver et al., 1999; Schuur and Matson, 2001). Similar oscillations, albeit at different frequencies, may be characteristic of near shore sediments (Aller, 1994). Temporally dynamic systems are characterized by persistent disequilibrium; chemical and biological characteristics associated with the *onset* of reducing or oxidizing conditions may persist until the next half-cycle is initiated.

4.3. Fe redox cycle evaluation

4.3.1. E_h, pH, and Fe_{aq}^{II} considerations

The observed oscillations in Fe^{II} concentration, E_h, and pH (Fig. 2) are consistent with the reduction reaction for labile Fe-oxide (e.g., Lindsay's "Soil-Fe"):

$$Fe(OH)_3(soil)_{(s)} + 3H^+ + e^- = Fe^{2+}_{(aq)} + 3H_2O$$
$$\log K^o = 15.74 \quad \text{(Lindsay, 1979)} \qquad (4)$$

where three moles of H^+ are consumed/produced per mole of Fe reduced/oxidized, and aqueous phase pH is buffered by other proton producing or consuming reactions including the oxidation of carbon (coupled to Fe reduction), the reduction of molecular oxygen (coupled to Fe oxidation), proton adsorption–desorption, and accessory solid phase dissolution–precipitation. The E_h range employed in this study is consistent with fluctuations observed during weekly E_h measurements in the field (Schuur and Matson, 2001). The concomitant fluctuation of pH is similar to that observed when an intact soil is subjected to oxic or anoxic conditions (data not shown). With respect to Lindsay's "soil-Fe", the reactor Fe^{II} activity oscillated between undersaturation during the reducing half-cycles and oversaturation during the oxidizing half-cycles. (Equilibrium saturation is indicated by the dashed line in Fig. 2.)

When we assume Fe reduction/oxidation is coupled to carbohydrate mineralization/oxygen reduction, the associated proton flux is reduced from three moles (as shown in Eq. (4)) to two moles. Using this approximation of two moles of protons for each mole of $[Fe^{2+}]_{<3\ kDa}$, we calculate that the total moles of protons consumed/produced during Fe reduction/oxidation was in excess (ca. 80 $mmol_c\ kg^{-1}$ soil) of measured pH shifts and known base additions. {One should note that a large portion (>70%) of the redox-active Fe^{II} resides within the operationally defined HCl-extractable pool (i.e., $[Fe^{II}]_{HCl}$). $[Fe^{II}]_{HCl}$ likely comprises Fe^{2+} ions adsorbed to surface hydroxyl sites and thus, as a first approximation, the proton flux resulting from fluctuations in $[Fe^{II}]_{HCl}$ is balanced by the two moles of proton adsorption–desorption necessary to maintain surface charge balance.} This excess proton flux suggests significant buffering by other soil processes such as mineral dissolution–precipitation or adsorption–desorption reactions. Accessory mineral dissolution at low pH was apparently not a major factor contributing to proton consumption during the oxidizing half-cycles as aqueous phase metals (e.g., $[Al]_{<3\ kDa}$) actually decreased at low pH. Rather, proton sorption–desorption at particle surfaces appears to be the principal source of pH buffering in this experiment. Proton buffering of a similar magnitude has been measured for Hawaiian soils of equivalent age (Chorover et al., 2004). These basaltic soils contain a high density of weakly acidic functional groups that apparently represent an effective buffer against the large proton flux that accompanies Fe cycling.

Aqueous Fe^{II} concentrations are a primary metric for evaluating the consistency of Fe redox cycles. Three prior experiments were deemed "unsuccessful" based on irregularities in this parameter and this motivated operational changes such as routine pH adjustment during the oxidizing half-cycles, normalization of DOC concentrations at the beginning of the reducing half-cycles, and "soil-Fe" equilibrium-based E_h targeting (see Section 2.5). In this experiment aqueous Fe^{II} concentrations were reasonably constant between cycles (Fig. 2C). The small variations observed cannot be attributed to the amount of C added, the pH at the start of the reducing half-cycle, or other operational parameters (data not shown). Rather, they likely result from minor variability in gas-flow rates, mixing rates, etc. between individual reactors.

4.3.2. Solid phase Fe distribution and mineral ripening

Distinct differences in Fe recovery by HCl and AAO extraction during the reducing and oxidizing half-cycles illustrates, perhaps more directly than before, the increase/decrease of extractable iron content with Fe reducing/oxidizing conditions (Quantin et al., 2002). According to Fig. 3, there is a portion of $[Fe^{II}]_{0.5\ M\ HCl}$ that is not oxidized under the experimental conditions; baseline $[Fe^{II}]_{<30\ nm\ +\ 0.\ 5\ M\ HCl}$ values return to ca. 20 $mmol\ kg^{-1}$ by the end of each oxidizing half-cycle. The Fe^{II} oxidation rate was greatest immediately following the addition of air into the reactors, tapering to below 1 $mmol\ kg^{-1}\ d^{-1}$ by the end of each oxidizing half-cycle. This is probably due to a depletion of readily oxidizable Fe^{II}.

Despite the expectation that rapid oxidation of Fe^{II} would result in precipitation of poorly crystalline (HCl-extractable) Fe^{III} solids (Stumm and Morgan, 1996), production of some fraction of non-HCl extractable Fe^{III} solid is also apparent (Fig. 3). For example, $[Fe^{II}]_{<30\ nm\ +\ 0.5\ M\ HCl}$ decreases from ca. 170 $mmol\ kg^{-1}$ at the end of the first reducing half-cycle (day 7, reactors A and B) to ca. 20 $mmol\ kg^{-1}$ at the end of the first oxidizing half-cycle (day 14, reactors A and B). If all of that Fe^{II} were oxidized to an HCl-extractable phase, then an increase in $[Fe^{III}]_{<30\ nm\ +\ 0.5\ M\ HCl}$ of ca. 150 $mmol\ kg^{-1}$ would be observed. However, the measured increase is 100 $mmol\ kg^{-1}$, or 66% of the total Fe^{II} oxidized. Furthermore, the amount of $[Fe^{II}]_{<30\ nm\ +\ 0.5\ M\ HCl}$ generated during reduction can not be completely accounted for by that lost from $[Fe^{III}]_{<30\ nm\ +\ 0.5\ M\ HCl}$. For example, the initial increase in $[Fe^{II}]_{<30\ nm\ +\ 0.5\ M\ HCl}$ of 50 (reactor B) or 85 (reactor A) $mmol\ kg^{-1}$ over the first reducing half-cycle is incompletely matched by the corresponding decreases in $[Fe^{III}]_{<30\ nm\ +\ 0.5\ M\ HCl}$ of 30 (reactor B) and 40 (reactor A) $mmol\ kg^{-1}$. Thus, while the HCl extraction is thought to probe the most labile Fe oxidation/reduction products, non-HCl extractable solids—produced during the oxidizing half-cycles and consumed during the reducing half-cycles—are important contributors to the short-term dynamics of our system.

All reactors show a slight downward trend in $[Fe^{III}]_{<30\ nm\ +\ 0.5\ M\ HCl}$ over the course of the experiment

(Fig. 3B). This trend is more evident when the AAO extractable mass is included, e.g., $[Fe^T]_{<30\ nm\ +\ 0.5\ M\ HCl\ +\ AAO}$ (Fig. 5B). This sum, termed $[Fe^T]_{SRO}$ henceforth, shows peaks at the end of each reducing half-cycle, similar to $[Fe^{III}]_{<30\ nm\ +\ 0.5\ M\ HCl}$. It is known that Fe^{II} can increase the rate of Fe-oxide dissolution in the presence of oxalate (Sulzberger et al., 1989). $[Fe^{II}]_{AAO}$ was not measured, but based on the known volume of $[Fe^{II}]_{HCl}$ remaining in the pellet, entrained Fe^{II} concentrations during the AAO extraction ranged from 70 to 700 μM, peaking at the end of the reducing half-cycles and following the general sinusoidal trend exhibited by $[Fe^{II}]_{HCl}$. This is within the range that (Sulzberger et al., 1989) found to accelerate Fe^{III}-oxide dissolution in the presence of oxalate. Since these entrained Fe^{II} concentrations span an order of magnitude, it is likely that part of the observed increase in total AAO extractable Fe during the reducing half-cycles is due to Fe^{II}-oxalate promoted dissolution. However, this does not explain the overall trend of decreasing $[Fe]_{SRO}$ as the experiment progressed. Entrained Fe^{II} concentrations, while increasing greatly during each reducing half-cycle, return to baseline values (ca. 70 μM) during each oxidizing half-cycle (data not shown). Furthermore, regression of entrained Fe^{II} concentration vs. AAO extractable Fe gave poor correlation ($R^2 = 0.3$) below 200 μM entrained Fe^{II}. Above this value, the correlation is improved only slightly ($R^2 = 0.5$).

The decrease in $[Fe]_{SRO}$ over the course of the experiment suggests that the kinetically labile Fe^{III}-oxide pool is being depleted. This refutes our initial hypothesis that oscillations in Fe redox status would promote the formation and retention of metastable SRO Fe-oxides. These wet chemical results are strongly supported by Mössbauer analysis of sample 1A (day 1) and 8C (day 56) from reactor B (Table 3 and Fig. 7). Using three different fitting models, the decrease in n-Gt (which is highly correlated with AAO extractable Fe, see Fig. 7 and Section 4.1) is consistent at 5.8% of total Fe (Table 3) while the absolute value of that Fe component varies from 33 to 39% of total Fe. The decrease in n-Gt as measured by Mössbauer spectroscopy is equal within error to the difference in $[Fe^T]_{SRO}$ of 6.4% of total Fe (Fig. 5). The Mössbauer results also reveal that Fe removed from the n-Gt component is transferred to the mc-Hm and mc-Gt components in roughly equal amounts (Table 3).

We propose that these redox cycles that induce alternate dissolution and precipitation of Fe^{III} solids, accelerate the Ostwald ripening process, promoting the formation of mc-Gt and mc-Hm over n-Gt. Comparable physico-chemical fluctuations have been used to accelerate the room temperature synthesis of dolomite and magnesite at the expense of their metastable counterparts (Deelman, 1999). Deelman (2001) argues that when formation of both metastable and stable mineral phases are possible thermodynamically, alternate dissolution and precipitation of the metastable phase will favor formation of the more stable phase. The mechanism whereby redox oscillations promote the formation of crystalline Fe-oxides at the expense of their SRO precursors may have its origins in the disequilibrium condition where Fe^{II} is sorbed at Fe^{III} mineral surfaces. This condition has been shown to expedite the kinetics of mineral ripening. For example, recent work has shown that Fe^{II} sorption to synthetic ferrihydrite promotes its rapid transformation to goethite (Hansel et al., 2003; Williams and Scherer, 2004; Pedersen et al., 2005). The rate of transformation may then result from the intensity (time × concentration) of Fe^{II} reaction with SRO Fe^{III} oxides, which in the present case is enhanced by redox oscillation.

4.3.3. Solubility product analysis

Lindsay and co-workers (Schwab and Lindsay, 1983; Brennan and Lindsay, 1998) have argued that metastable equilibrium is maintained, even over short times in dynamic systems such as soils, by poorly ordered transitory phases. They suggest that Fe^{II} activity is controlled by mixed-valence amorphous Fe-oxides (MVA Fe-oxides) with solubility relations that resemble hydrated-magnetite (Schwab and Lindsay, 1983). Under the assumption of metastable equilibrium, the stoichiometry of mineral species controlling Fe^{II} activity may be inferred from the slope of the data plotted as [pE + pH] versus $[\log(Fe^{2+}) + 2\ pH]$. While equilibrium with an Fe^{III} mineral (e.g., goethite) yields a slope of −1, magnetite ($Fe^{II}Fe^{III}{}_2O_4$) gives a slope of −0.67. Linear regression of data compiled from all three of our replicate reactors yields a slope of −0.66 and an intercept of 13.6, also consistent with the MVA Fe-oxide model (Fig. 11). Although only a relatively small mass of MVA Fe-oxide would be required to control Fe^{2+} solubility, no direct evidence (i.e., TEM or spectroscopic data) in our study or in prior studies (Schwab and Lindsay, 1983; Brennan and Lindsay, 1998) documents their presence.

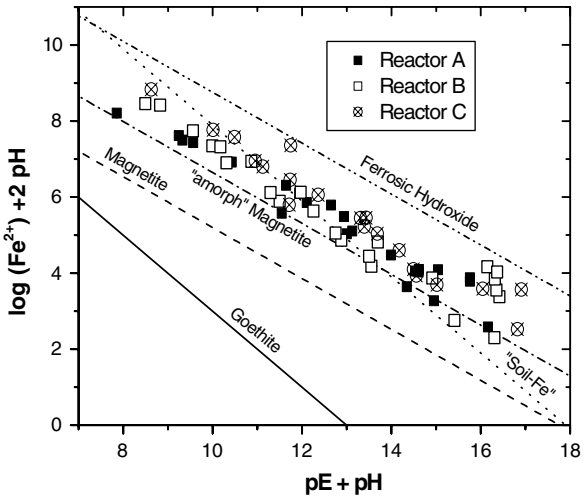

Fig. 11. Solubility diagram for $[Fe^{II}]_{<3\ kDa}$ for all reactors at the pH and E_h values shown in Fig. 2. Solubility relations for minerals were calculated from dissolution thermodynamic data for goethite, "soil-Fe"—$Fe(OH)_3$ and magnetite (Lindsay, 1979) and "amorp" magnetite and ferrosic hydroxide (Brennan and Lindsay, 1998).

Furthermore, the activities of Fe^{2+} and H^+, and therefore the slope of the best fit line in Fig. 11, are also affected by Fe^{2+} adsorption–desorption equilibria, which can be represented by:

$$\equiv S{-}OH + Fe^{2+}{}_{(aq)} \leftrightarrow \equiv S{-}O{-}Fe^{+} + H^{+}{}_{(aq)} \quad (5)$$

where ≡SOH is a particle surface hydroxyl group. Surface adsorption of Fe^{2+} would diminish $Fe^{2+}{}_{(aq)}$ and the associated displacement of protons would decrease pH. When plotted on Fig. 11, surface adsorption of Fe^{2+} would produce a larger (less negative) slope than a corresponding scenario in which no adsorption of Fe^{2+} occurs. Thus, adsorption–desorption of Fe^{2+} could buffer the aqueous phase response to Fe^{III}-oxide dissolution–precipitation giving rise to the non-unity slope in Fig. 11 that previously has been attributed exclusively to MVA Fe oxides. Because of this ambiguity regarding the impact of surface adsorbed Fe^{2+}, standard thermodynamic predictions that redox-dynamic soils are in equilibrium with mixed Fe^{II}–Fe^{III} solids must be interpreted cautiously.

4.3.4. Fe reduction/oxidation rates

Our initial hypothesis was that multiple Fe redox oscillations would result in increased rates of Fe reduction as microbial communities became more adapted to the specific oscillating conditions of the experiment. However, we found that Fe reduction rates, inferred from the rate of increase in $[Fe^{II}]_{<30\ nm\ +\ 0.5\ M\ HCl}$, were similar during each reducing half-cycle (Fig. 6). Not all solid-phase Fe^{II} minerals are solubilized by the 0.5 M HCl extraction (e.g., magnetite is not extracted; Kostka and Luther, 1994), and thus if non-HCl extractable Fe^{II} minerals exhibit dissolution–precipitation dynamics in these experiments, then the reported Fe reduction and oxidation rates could be underestimated. However, the only Fe^{II} mineral detected by MBS was ilmenite ($FeTiO_3$); magnetite was not detected. Furthermore, although $[Fe^{II}]_{AAO}$ was not measured routinely, separate studies with this soil indicated that all detected $[Fe^{II}]_{AAO}$ could be accounted for by entrained $[Fe^{II}]_{HCl}$ (data not shown). Thus, the Fe reduction rates are a reasonable approximation, whereas the Fe oxidation rates are likely underestimated; mass-balance (Section 4.3.2) and Mössbauer (Section 4.1) data provide clear evidence that non-HCl extractable Fe^{III}-oxides take part in dissolution–precipitation dynamics in this system.

Because we placed rather strict geochemical constraints on the Fe redox cycles (see Section 2.5), the similarity of Fe reduction rates throughout the course of the experiment could reflect control by physico-chemical conditions rather than by adaptations of microbial catalysis. It may also be that the sampling frequency (1, 4, and 7 d after initiation of an oxidation or reduction half-cycle) was insufficient to resolve rate dynamics that were operative at shorter time scales. Nonetheless, the initially high Fe oxidation rates in the first day of all oxidizing half-cycles followed by their subsequent decrease are consistent with aqueous Fe^{II} and pH control.

4.3.5. Solid phase behavior of Al, Si, and Ti

The degree to which the major framework metals (Fe, Al, Si, and Ti) are altered by redox cycling is of considerable importance to soil structure and nutrient availability. While values of $[Fe]_{HCl}$ and $[Fe]_{AAO}$ exceed those of any other metal, $[Al]_{AAO}$:$[Fe]_{AAO}$ and $[Ti]_{AAO}$:$[Fe]_{AAO}$ are consistently 0.3 and 0.4, respectively, throughout the experiment; thus, redox cycling impacts the structural stability or ''lability'' of Al and Ti bearing minerals. The relative consistency of the molar ratio of Fe:Al:Ti of ca. 2:1:1 despite intra-cycle fluctuations in $[Fe]_{AAO}$, $[Al]_{AAO}$, and $[Ti]_{AAO}$ suggests a common source. SRO Fe and Al are abundant in these soils, Fe-Ti primary minerals have been noted in Hawaiian basalt (Golden et al., 1993) and ilmenite has been detected in this soil ($FeTiO_3$) by MBS (Figs. 7 and 8; Table 2). Oxidation of Fe^{II} in the presence of Al is known to produce mixed Fe-Al solids, such as aluminous goethite (Fey and Dixon, 1981). The highly collapsed pattern of the LHeT Mössbauer spectra is indicative of Al-substituted goethites and may also indicate Ti substitution as well. Although, Ti substitution is more commonly observed in hematite (Trolard et al., 1995), Ti-bearing goethites have also been reported (Fitzpatrick et al., 1978; Tessens and Zauyah, 1982). Metal–organic complexes, which are known to be prevalent these types of soils (Chorover et al., 2004), may also play an important role in regulating the composition of HCl and AAO extractable Fe, Al and Ti.

5. Conclusions

Two week cycles in redox status (across the ''soil-Fe'' reductive dissolution boundary) over an eight week period produced pronounced intra-cycle changes (reducing vs. oxidizing conditions) in aqueous and HCl extractable Fe^{II} and Fe^{III}, as well as HCl and AAO extractable Fe^{T}, Al, Si, and Ti. After four cycles, several cumulative effects were also apparent, the most prominent being an increase in the crystalline-character of Fe-minerals, quantified on the basis of both wet chemistry and Mössbauer spectroscopy. Mössbauer data indicated the transformation of (Al-bearing) nano-goethite to micro-crystalline (mc-) hematite and mc-goethite. This transformation is reflected macroscopically in the time-dependent decrease in $[Fe]_{SRO}$ over the course of the experiment. An observed concomitant decrease in $[Al]_{SRO}$ may indicate significant Al-substitution within SRO Fe-oxides.

These results indicate that some geochemical features of Fe redox cycling become apparent only after several consecutive redox cycles. In environments that are subjected to variations in redox status, the frequency of redox shifts may influence soil mineral transformation. Intermittent periods of anoxia are commonly thought to cause a depletion of $[Fe]_{SRO}$ via reduction and removal due to leaching, thus enriching the remaining soil in crystalline Fe-oxides by mass balance (e.g. Miller et al., 2001). Here we have shown that redox oscillations that span the Fe reduction/oxidation threshold can promote the direct conversion of SRO material into

more crystalline forms (e.g., goethite and hematite) with no Fe removal, thereby providing an alternative pathway for mineral transformation during pedogenesis. Our experiments were conducted in closed systems and thus represent an end member scenario with no leaching.

Acknowledgments

We thank Peter Vitousek for his leadership on the Hawaii Ecosystems Project, Heraldo Ferrington for logistical and sampling assistance in the field and Mary Kay Amistadi for ICP-MS analysis. This project was supported by National Research Initiative Competitive Grant No. 2003-35107-13663 from the USDA Cooperative State Research, Education, and Extension Service; National Science Foundation Grant No. DEB-0212245; and The Pennsylvania State University BRIE (IGERT) Grant No. DGE-9972759. The Mössbauer measurements were funded by a Strategic Project Grant from the Natural Sciences and Engineering Research Council of Canada to co-author D.G.R. Finally, we thank Daniel Richter and two anonymous reviewers for helpful comments on the manuscript.

Associate editor: Carrick M. Eggleston

Appendix A

See Tables A1 and A2.

Table A1
Fitting and calculated Mossbauer parameters for the RT spectra

Sample	Fit	BG (MC/ch)	Phase	Delta-0 (mm/s)	Area (MC.mm/s)	Epsilon-0 (mm/s)	*p* (%)	DELTA or *z* (mm/s)	Sigma (mm/s)	Chi-2-red (epsilon-1)	⟨CS⟩ (mm/s)	⟨Eps⟩ (mm/s)	⟨*z*⟩ or ⟨QS⟩ (mm/s)	SD (mm/s)
1A	I-q	8.53094*	Q	0.3689	1.057	n/a	49.3*	0.881	0.272	5.8	0.3689	n/a	0.716	0.277
							50.7	0.555	0.165					
			mc-Hm	0.3499	0.251	−0.0933	46.5*	3.38	0.085		0.3499	−0.0933	3.251	0.196
							53.5	3.138	0.197					
			mc-Gt	0.37*	0.333	−0.156	100*	2.315	0.556		0.37*	−0.156	2.315	0.556
			b-Gt	0.617	0.65	0.271	100*	0*	0.502		0.617	0.27	0.401	0.303
V3	I-h	11.8627*	Q	0.3735	1.319	n/a	52.9*	0.866	0.252	6.8	0.373	n/a	0.717	0.262
							47.1	0.549	0.146					
			mc-Hm	0.3599	0.281	−0.1001	46.1*	3.402	0.079		0.3599	−0.1001	3.266	0.195
							53.9	3.151	0.189					
			mc-Gt	0.37*	0.433	−0.199	100*	2.304	0.579		0.37*	−0.199	2.304	0.579
			b-Gt	0.619	0.861	0.271	100*	0*	0.493		0.619	0.271	0.395	0.299
8C	I-d	7.54081*	Q	0.3742	0.7384	n/a	51.5*	0.874	0.255	4.7	0.3742	n/a	0.7197	0.263
							48.5	0.556	0.149					
			mc-Hm	0.3637	0.226	−0.0948	50.2*	3.374	0.098		0.3637	−0.0948	3.232	0.223
							49.8	3.091	0.223					
			mc-Gt	0.37*	0.282	−0.208	100*	2.257	0.579		0.37*	−0.208	2.257	0.579
			b-Gt	0.647	0.5812	0.281	100*	0*	0.499		0.647	0.281	0.398	0.301
1A	II-s	8.53094*	Q	0.367	1.151	n/a	38.7*	0.94	0.328	3.28	0.367	n/a	0.717	0.317
							61.3	0.578	0.219					
			il	1.031	0.0542	n/a	100*	0.773	0.082		1.031	n/a	0.773	0.082
			mc-Hm	0.366	0.261	−0.1064	48.7*	3.369	0.092		0.366	−0.1064	3.225	0.227
							51.3	3.088	0.232					
			mc-Gt	0.37*	0.471	−0.166	100*	1.895	1.122		0.37*	−0.166	1.937	1.048
			b-Gt	0.585	0.366	0.364	100*	0*	0.411		0.585	0.364	0.328	0.248
V3	II-k	1.18627*	Q	0.3695	1.401	n/a	47.9*	0.89	0.306	3.6	0.3695	n/a	0.723	0.299
							52.1	0.57	0.192					
			il	1.034	0.0677	n/a	100*	0.754	0.094		1.034	n/a	0.754	0.0939
			mc-Hm	0.377	0.342	−0.115	46.3*	3.381	0.0996		0.377	−0.115	3.201	0.273
							53.7	3.045	0.28					
			mc-Gt	0.37*	0.607	−0.556	100*	1.58	1.102		0.37*	−0.556	1.654	0.986
			b-Gt	0.476	0.48	0.259	100*	0*	0.365		0.476	0.259	0.291	0.219
8C	II-g	7.54081*	Q	0.3684	0.817	n/a	38.2*	0.95	0.324	2.17	0.3684	n/a	0.726	0.314
							61.8	0.589	0.216					
			il	1.037	0.0436	n/a	100*	0.764	0.104		1.037	n/a	0.764	0.104
			mc-Hm	0.379	0.265	−0.1098	47.1*	3.362	0.109		0.379	−0.1098	3.179	0.288
							52.9	3.017	0.301					
			mc-Gt	0.37*	0.418	−0.582	100*	1.46	1.114		0.37*	−0.582	1.558	0.971
			b-Gt	0.527	0.285	0.315	100*	0*	0.356		0.527	0.315	0.284	0.215
1A	III-*z*	8.53094*	Q	0.3665	1.174	n/a	39.1*	0.911	0.314	1.88	0.3665	n/a	0.702	0.305
							60.9	0.571	0.214					
			il	1.016	0.0394	n/a	100*	0.781	0.083		1.016	n/a	0.781	0.0829
			mc-Hm	0.356	0.241	−0.0971	47.7*	3.379	0.083		0.356	−0.0971	3.253	0.194

(*continued on next page*)

Table A1 (*continued*)

Sample	Fit	BG (MC/ch)	Phase	Delta-0 (mm/s)	Area (MC.mm/s)	Epsilon-0 (mm/s)	*p* (%)	DELTA or *z* (mm/s)	Sigma (mm/s)	Chi-2-red (epsilon-1)	⟨CS⟩ (mm/s)	⟨Eps⟩ (mm/s)	⟨*z*⟩ or ⟨QS⟩ (mm/s)	SD (mm/s)
							52.3	3.137	0.194					
			mc-Gt	0.37*	0.386	−0.036	100*	2.216	0.755		0.37*	−0.0361	2.217	0.753
			b-Gt	0.572	0.452	0.338	100*	0.353	0.354	(−0.468)	0.572	0.173	0.412	0.283
V3	III-o	11.8627*	Q	0.3733	1.433	n/a	55.2*	0.821	0.297	1.99	0.3733	n/a	0.701	0.284
							44.8	0.551	0.181					
			il	1.022	0.0365	n/a	100*	0.776	0.037		1.022	n/a	0.776	0.037
			mc-Hm	0.3676	0.295	−0.1052	46.7*	3.394	0.086		0.3676	−0.1052	3.245	0.221
							53.3	3.115	0.219					
			mc-Gt	0.37*	0.524	−0.188	100*	1.977	0.841		0.37*	−0.188	1.982	0.829
			b-Gt	0.567	0.601	0.248	100*	0.351	0.262	(−0.256)	0.567	0.159	0.373	0.229
8C	III-L	7.54081*	Q	0.3757	0.829	n/a	37.6*	0.911	0.321	1.51	0.3757	n/a	0.704	0.302
							62.4	0.581	0.216					
			il	1.022	0.0335	n/a	100*	0.776	0.093		1.022	n/a	0.776	0.093
			mc-Hm	0.3708	0.243	−0.0999	49.5*	3.366	0.105		0.3708	−0.0999	3.202	0.259
							50.5	3.041	0.266					
			mc-Gt	0.37*	0.401	−0.262	100*	1.681	1.018		0.37*	−0.262	1.721	0.945
			b-Gt	0.593	0.321	0.256	100*	0.345	0.218	(−0.188)	0.593	0.191	0.356	0.201

Note. All fits performed using the Voigt-based fitting method of Rancourt and Ping (1991) with the Recoil software developed in co-author Rancourt's laboratory. All fitting and calculated parameters are as defined in by Rancourt and Ping (1991). *This parameter frozen or constrained during fit. Lorentzian half widths at half maximum (HWHM) of all elemental Lorentzians in all elemental doublet and sextets were all frozen at the (twice) Heisenberg value of 0.097 mm/s. All delta-1 couplings between CS and *z* (or DELTA) were taken to be zero. All line-1 to line-2 area ratios in all (distributed) elemental doublets were taken to be 1. All line-2/line-3 and line-1/line-3 area ratios in all (distributed and symmetric) elemental sextets were taken to be 2 and 3, respectively. All epsilon-1 couplings between epsilon and *z* (in a HFD) are taken to be 0, except for the b-Gt spectral component where it is allowed to adjust. BG = backbround level, in mega-counts per channel (MC/ch). phase = assigned spectral component, as described in the text. DELTA = the center (or position) of a Gaussian component in the quadrupole splitting distribution (QSD) of a given doublet spectral component. *z* = the center (or position) of a Gaussian component in the hyperfine field distribution (HFD) of a given 'sextet' spectral component. sigma = the Gaussian SD width of a given Gaussian component of a given QSD or HFD. *p* (in %) is the weigt factor for a given Gaussian component in a given QSD or HFD. ⟨*A*⟩ signifies the average of the absolute value of *A*. ⟨*z*⟩ is the average magnitude of the hyperfine field (expressed as an excited state Zeeman splitting, in mm/s) in a given HFD of a given sextet spectral component. ⟨QS⟩ is the average magnitude of the quadrupole splitting in a given QSD of a given doublet spectral component. ⟨Eps⟩ is the average magnitude of the slave distribution of quadrupole shifts (epsilons) associated to a given HFD of a given sextet spectral component. SD is the standard deviation width of a given distribution (QSD, HFD, or slave distributions) chi-2-red is the reduced chi-squared value for the fit: chi-squared divided by the number of degrees of freedom. It has an ideal value of 1 for a correct model. All center shifts (CSs, delta-0, ⟨CS⟩) are given with respect to the CS of metallic Fe at RT.

Table A2
Fitting and calculated Mossbauer parameters for the LHeT spectra

Sample	Fit	BG (MC/ch)	Phase	Delta-0 (mm/s)	Area (MC.mm/s)	Epsilon-0 (mm/s)	*p* (%)	DELTA or *z* (mm/s)	Sigma (mm/s)	*A*-2/*A*-3	*A*-1/*A*-3	Chi-2-red (epsilon-1)	⟨CS⟩ (mm/s)	⟨Eps⟩ (mm/s)	⟨*z*⟩ or ⟨QS⟩ (mm/s)	SD (mm/s)
1A	n	1.54766*	Q′	0.495	0.0462	n/a	100*	0.796	0.409	n/a	n/a	2.08	0.495	n/a	0.804	0.393
			mc-Hm	0.493	0.0424	−0.0993	100*	3.547	0.09	2*	3*		0.493	−0.0993	3.547	0.09
			mc + b-Gt	0.471	0.146	−0.118	48.3*	3.347	0.077	3.04	4.98		0.471	−0.118	3.232	0.229
							51.7	3.124	0.268							
			n-Gt	0.66	0.1355	0.21	100*	0*	2.14	2*	3*		0.66	0.21	1.708	1.29
V3	ee	1.2492*	Q′	0.495	0.0377	n/a	100*	0.765	0.371	n/a	n/a	1.77	0.495	n/a	0.77	0.36
			mc-Hm	0.493	0.0283	−0.093	100*	3.549	0.069	2*	3*		0.493	−0.093	3.549	0.0688
			mc + b-Gt	0.468	0.141	−0.114	50.3*	3.341	0.0778	2.76	4.45		0.468	−0.114	3.228	0.232
							49.7	3.113	0.275							
			n-Gt	0.699	0.1022	0.22	100*	0.8	1.76	2*	3*		0.699	0.22	1.54	1.16
8C	nn	1.1326	Q′	0.494	0.0403	n/a	100*	0.777	0.384	n/a	n/a	1.86	0.494	n/a	0.783	0.371
			mc-Hm	0.496	0.029	−0.0918	100*	3.564	0.069	2*	3*		0.496	−0.0918	3.564	0.069
			mc + b-Gt	0.473	0.116	−0.1161	47.8*	3.36	0.082	2.8	4.5		0.473	−0.1161	3.277	0.233
							52.2	3.201	0.292							
			n-Gt	0.795	0.1011	0.36	100*	0.01	2.1	2*	3*		0.795	0.36	1.68	1.27

Note. All fits performed using the Voigt-based fitting method of Rancourt and Ping (1991) with the Recoil software developed in co-author Rancourt's laboratory. All fitting and calculated parameters are as defined in by Rancourt and Ping (1991). *This parameter frozen or constrained during fit. Lorentzian half widths at half maximum (HWHM) of all elemental Lorentzians in all elemental doublet and sextets were all frozen at the (twice) Heisenberg value of 0.097 mm/s. All delta-1 couplings between CS and *z* (or DELTA) were taken to be zero. All line-1 to line-2 area ratios in all (distributed) elemental doublets were taken to be 1. All epsilon-1 couplings between epsilon and *z* (in a HFD) are taken to be 0. BG = backbround level, in mega-counts per channel (MC/ch). phase = assigned spectral component, as described in the text. DELTA = the center (or position) of a Gaussian component in the quadrupole splitting distribution (QSD) of a given doublet spectral component. *z* = the center (or position) of a Gaussian component in the hyperfine field distribution (HFD) of a given 'sextet' spectral component. sigma = the Gaussian SD width of a given Gaussian component of a given QSD or HFD. *p* (in %) is the weigt factor for a given Gaussian component in a given QSD or HFD. Line-2/line-3 and line-1/line-3 area ratios in all (distributed and symmetric) elemental sextets are denoted *A*-2/*A*-3 and *A*-1/*A*-3, respectively. ⟨*A*⟩ signifies the average of the absolute value of *A*. ⟨*z*⟩ is the average magnitude of the hyperfine field (expressed as an excited state Zeeman splitting, in mm/s) in a given HFD of a given sextet spectral component. ⟨QS⟩ is the average magnitude of the quadrupole splitting in a given QSD of a given doublet spectral component. ⟨Eps⟩ is the average magnitude of the slave distribution of quadrupole shifts (epsilons) associated to a given HFD of a given sextet spectral component. SD is the standard deviation width of a given distribution (QSD, HFD, or slave distributions) chi-2-red is the reduced chi-squared value for the fit: chi-squared divided by the number of degrees of freedom. It has an ideal value of 1 for a correct model. All center shifts (CSs, delta-0, ⟨CS⟩) are given with respect to the CS of metallic Fe at RT.

References

Aller, R.C., 1994. Bioturbation and remineralization of sedimentary organic matter: Effects of redox oscillation. *Chem. Geol.* **114**, 331–345.

Aller, R.C., Mackin, J.E., Cox, R.T., 1986. Diagenesis of Fe and S in Amazon inner shelf muds: Apparent dominance of Fe reduction and implications for the genesis of ironstones. *Cont. Shelf Res.* **6**, 263–289.

Anschutz, P., Sundby, B., Lefrancois, L., Luther, G.W., Mucci, A., 2000. Interactions between metal oxides and species of nitrogen and iodine in bioturbated marine sediments. *Geochim. Cosmochim. Acta* **64**, 2751–2763.

Bonneville, S., Van Cappellen, P., Behrends, T., 2004. Microbial reduction of iron(III) oxyhydroxides: Effects of mineral solubility and availability. *Chem. Geol.* **212**, 255–268.

Brennan, E.W., Lindsay, W.L., 1998. Reduction and oxidation effect on the solubility and transformation of iron oxides. *Soil Sci. Soc. Am. J.* **62**, 930–937.

Caradec, S., Grossi, V., Gilbert, F., Guigue, C., Goutx, M., 2004. Influence of various redox conditions on the degradation of microalgal triacylglycerols and fatty acids in marine sediments. *Org. Geochem.* **35**, 277–287.

Chadwick, O.A., Chorover, J., 2001. The chemistry of pedogenic thresholds. *Geoderma* **100**, 321–353.

Chorover, J., Amistadi, M.K., Chadwick, O.A., 2004. Surface charge evolution of mineral–organic complexes during pedogenesis in Hawaiian basalt. *Geochim. Cosmochim. Acta* **68**, 4859–4876.

Cornell, R.M., Schwertmann, U., 1996. The iron oxides: Soils (Chapter 16). In: Cornell, R.M., Schwertmann, U. (Eds.), *The Iron Oxides*. VCH, pp. 395–432.

Dang, M.Z., Rancourt, D.G., Dutrizac, J.E., Lamarche, G., Provencher, R., 1998. Interplay of surface conditions, particle size, stoichiometry, cell parameters, and magnetism in synthetic hematite-like materials. *Hyperfine Interact.* **117**, 271–319.

Deelman, J.C., 1999. Low-temperature nucleation of magnesite and dolomite. *Neus Jb. Miner. Monat.*, 289–302.

Deelman, J.C., 2001. Breaking Ostwald's rule. *Chem. Erde-Geochem.* **61**, 224–235.

Fey, M.V., Dixon, J.B., 1981. Synthesis and properties of poorly crystalline hydrated aluminous goethites. *Clay Clay Miner.* **29**, 91–100.

Fitzpatrick, R.W., Leroux, J., Schwertmann, U., 1978. Amorphous and crystalline titanium and iron–titanium oxides in synthetic preparations, at near ambient conditions, and in soil clays. *Clay Clay Miner.* **26**, 189–201.

Flessa, H., Fischer, W.R., 1992. Plant-induced changes in the redox potentials of rice rhizospheres. *Plant Soil* **143**, 55–60.

Frenzel, P., Bosse, U., Janssen, P.H., 1999. Rice roots and methanogenesis in a paddy soil: Ferric iron as an alternative electron acceptor in the rooted soil. *Soil Biol. Biochem.* **31**, 421–430.

Golden, D.C., Morris, R.V., Ming, D.W., Lauer, H.V., Yang, S.R., 1993. Mineralogy of 3 slightly palagonitized basaltic tephra samples from the summit of Mauna-Kea, Hawaii. *J. Geophys. Res.—Planets* **98**, 3401–3411.

Gotoh, S., Patrick, W.H., 1974. Transformation of iron in a waterlogged soil as influenced by redox potential and pH. *Soil Sci. Soc. Am. J.* **38**, 66–71.

Hansel, C.M., Benner, S.G., Neiss, J., Dohnalkova, A., Kukkadapu, R.K., Fendorf, S., 2003. Secondary mineralization pathways induced by dissimilatory iron reduction of ferrihydrite under advective flow. *Geochim. Cosmochim. Acta* **67**, 2977–2992.

Hossner, L.R., 1996. Dissolution for total elemental analysis. In: Sparks, D.L. (Ed.), *Methods of Soil Analysis: Part 3—Chemical Methods*. Soil Science Society of America, pp. 49–64.

King, G.M., Garey, M.A., 1999. Ferric iron reduction by bacteria associated with the roots off freshwater and marine macrophytes. *Appl. Environ. Microbiol.* **65**, 4393–4398.

Kirk, G., 2004. Reduction and oxidiation. In: Kirk, G. (Ed.), *The Biogeochemistry of Submerged Soils*. John Wiley & Sons, Ltd, pp. 93–134.

Komada, T., Reimers, C.E., Luther III, G.W., Burdige, D.J., 2004. Factors affecting dissolved organic matter dynamics in mixed-redox to anoxic coastal sediments. *Geochim. Cosmochim. Acta* **68**, 4099–4111.

Kostka, J.E., Luther, G.W., 1994. Partitioning and speciation of solid-phase iron in salt-marsh sediments. *Geochim. Cosmochim. Acta* **58**, 1701–1710.

Lalonde, A.E., Rancourt, D.G., Ping, J.Y., 1998. Accuracy of ferric/ferrous determinations in micas: A comparison of mossbauer spectroscopy and the pratt and wilson wet-chemical methods. *Hyperfine Interact.* **117**, 175–204.

Liang, L.Y., Mccarthy, J.F., Jolley, L.W., Mcnabb, J.A., Mehlhorn, T.L., 1993. Iron dynamics: Transformation of Fe(II)/Fe(III) during injection of natural organic-matter in a sandy aquifer. *Geochim. Cosmochim. Acta* **57**, 1987–1999.

Lindsay, W.L., 1979. Iron. In: Lindsay, W.L. (Ed.), *Chemical Equilibria in Soils*. John Wiley & Sons, pp. 129–149.

Loeppert, R.H., Inskeep, W.P., 1996. Iron. In: Sparks, D.L. (Ed.), *Methods of Soil Analysis: Part 3—Chemical Methods*. Soil Science Society of America, pp. 639–664.

Lovley, D.R., Phillips, E.J.P., 1986. Organic-matter mineralization with reduction of ferric iron in anaerobic sediments. *Appl. Environ. Microbiol.* **51**, 683–689.

Majcher, E.H., Chorover, J., Bollag, J.M., Huang, P.M., 2000. Evolution of CO_2 during birnessite-induced oxidation of C-14-labeled catechol. *Soil Sci. Soc. Am. J.* **64**, 157–163.

Miller, A.J., Schuur, E.A.G., Chadwick, O.A., 2001. Redox control of phosphorus pools in Hawaiian montane forest soils. *Geoderma* **102**, 219–237.

Murad, E., Cashion, J., 2004. Metastable materials (Chapter 9). In: *Mössbauer Spectroscopy of Environmental Materials and their Industrial Utilization*. Kluwer Academic Publishers Group, pp. 241–253.

Parfitt, R.L., Childs, C.W., Eden, D.N., 1988. Ferrihydrite and allophane in four andepts from Hawaii and implications for their classification. *Geoderma* **41**, 223–241.

Patrick, W., Williams, B., Moraghan, J., 1973. A simple system for controlling redox potential and pH in soil suspensions. *Soil Sci. Soc. Am. Proc.* **37**, 331–332.

Patrick, W.H., Henderson, R.E., 1981. Reduction and reoxidation of manganese and iron in flooded soil and in water solution. *Soil Sci. Soc. Am. J.* **45**, 855–859.

Patrick, W.H., Jugsujinda, A., 1992. Sequential reduction and oxidation of inorganic nitrogen, manganese, and iron in flooded soil. *Soil Sci. Soc. Am. J.* **56**, 1071–1073.

Pedersen, H.D., Postma, D., Jakobsen, R., Larsen, O., 2005. Fast transformation of iron oxyhydroxides by the catalytic action of aqueous Fe(II). *Geochim. Cosmochim. Acta* **69**, 3967–3977.

Petrie, R.A., Grossl, P.R., Sims, R.C., 1998. Controlled environment potentiostat to study solid–aqueous systems. *Soil Sci. Soc. Am. J.* **62**, 379–382.

Pullin, M.J., Cabaniss, S.E., 2003. The effects of pH, ionic strength, and iron–fulvic acid interactions on the kinetics of nonphotochemical iron transformations. I. Iron(II) oxidation and iron(III) colloid formation. *Geochim. Cosmochim. Acta* **67**, 4067–4077.

Quantin, C., Becquer, T., Rouiller, J.H., Berthelin, J., 2001. Oxide weathering and trace metal release by bacterial reduction in a New Caledonia Ferralsol. *Biogeochemistry* **53**, 323–340.

Quantin, C., Becquer, T., Rouiller, J.H., Berthelin, J., 2002. Redistribution of metals in a New Caledonia Ferralsol after microbial weathering. *Soil Sci. Soc. Am. J.* **66**, 1797–1804.

Rancourt, D.G., 1998. Mossbauer spectroscopy in clay science. *Hyperfine Interact.* **117**, 3–38.

Rancourt, D.G., McDonald, A.M., Lalonde, A.E., Ping, J.Y., 1993. Mossbauer absorber thicknesses for accurate site populations in Fe-bearing minerals. *Am. Mineral.* **78**, 1–7.

Rancourt, D.G., Ping, J.Y., 1991. Voigt-based methods for arbitrary-shape static hyperfine parameter distributions in mossbauer-spectroscopy. *Nucl. Instrum. Methods Phys. Res., Sect. B* **58**, 85–97.

Rancourt, D.G., Thibault, P.-J., Mavrocordatos, D., Lamarche, G., 2005. Hydrous ferric oxide precipitation in the presence of nonmetabolizing bacteria: Constraints on the mechanism of a biotic effect. *Geochim. Cosmochim. Acta* **69**, 553–577.

Reddy, K.R., Patrick, W.H., 1975. Effect of alternate aerobic and anaerobic conditions on redox potential, organic-matter decomposition and nitrogen loss in a flooded soil. *Soil Biol. Biochem.* **7**, 87–94.

Reddy, K.R., Patrick, W.H., Lindau, C.W., 1989. Nitrification–denitrification at the plant root–sediment interface in wetlands. *Limnol. Oceanogr.* **34**, 1004–1015.

Roden, E., 2003. Fe(III) oxide reactivity toward biological versus chemical reduction. *Environ. Sci. Technol.* **37**, 1319–1324.

Roden, E., Sobolev, D., Glazer, B., Luther, G., 2004. Potential for microscale bacterial Fe redox cycling at the aerobic–anaerobic interface. *Geomicrobiol. J.* **21**, 379–391.

Roden, E.E., 2004. Analysis of long-term bacterial vs. chemical Fe(III) oxide reduction kinetics. *Geochim. Cosmochim. Acta* **68**, 3205–3216.

Schuur, E.A.G., Matson, P.A., 2001. Net primary productivity and nutrient cycling across a mesic to wet precipitation gradient in Hawaiian montane forest. *Oecologia* **128**, 431–442.

Schwab, A.P., Lindsay, W.L., 1983. Effect of redox on the solubility and availability of iron. *Soil Sci. Soc. Am. J.* **47**, 201–205.

Shoji, S., Nanzyo, M., Dahlgren, R.A., 1993. *Volcanic Ash Soils: Genesis, Properties and Utilization*. Elsevier.

Silver, W.L., Lugo, A.E., Keller, M., 1999. Soil oxygen availability and biogeochemistry along rainfall and topographic gradients in upland wet tropical forest soils. *Biogeochemistry* **44**, 301–328.

Steefel, C.I., Van Cappellen, P., 1990. A new kinetic approach to modeling water–rock interaction: The role of nucleation, precursors, and Ostwald ripening. *Geochim. Cosmochim. Acta* **54**, 2657–2677.

Stookey, L., 1970. Ferrozine: A new spectrophotometric reagent for iron. *Anal. Chem.* **42**, 779–781.

Stumm, W., Morgan, J.J., 1996. Nucleation and crystal growth (Chapter 13.7). In: Schnoor, J.L., Zehnder, A. (Eds.), *Aquatic Chemistry: Chemical Equilibrium and Rates in Natural Waters*. John Wiley & Sons, Inc, pp. 800–817.

Sulzberger, B., Suter, D., Siffert, C., Banwart, S., Stumm, W., 1989. Dissolution of Fe(III)(hydr)oxides in natural waters; laboratory assessment on the kinetics controlled by surface coordination. *Mar. Chem.* **28**, 127–144.

Tessens, E., Zauyah, S., 1982. Positive permanent charge in oxisols. *Soil Sci. Soc. Am. J.* **46**, 1103–1106.

To, T.B., Nordstrom, D.K., Cunningham, K.M., Ball, J.W., McCleskey, R.B., 1999. New method for the direct determination of dissolved Fe(III) concentration in acid mine waters. *Environ. Sci. Technol.* **33**, 807–813.

Trolard, F., Bourrie, G., Jeanroy, E., Herbillon, A.J., Martin, H., 1995. Trace-metals in natural iron-oxides from laterites: A study using selective kinetic extraction. *Geochim. Cosmochim. Acta* **59**, 1285–1297.

Van Cappellen, P., Viollier, E., Roychoudhury, A., Clark, L., Ingall, E., Lowe, K., Dichristina, T., 1998. Biogeochemical cycles of manganese and iron at the oxic–anoxic transition of a stratified marine basin (Orca Basin, Gulf of Mexico). *Environ. Sci. Technol.* **32**, 2931–2939.

Van Der Zee, C., Roberts, D.R., Rancourt, D.G., Slomp, C.P., 2003. Nanogoethite is the dominant reactive oxyhydroxide phase in lake and marine sediments. *Geology* **31**, 993–996.

Viollier, E., Inglett, P.W., Hunter, K., Roychoudhury, A.N., Van Cappellen, P., 2000. The ferrozine method revisited: Fe(II)/Fe(III) determination innatural waters. *Appl. Geochem.* **15**, 785–790.

Washington, J.W., Endale, D.M., Samarkina, L.P., Chappell, K.E., 2004. Kinetic control of oxidation state at thermodynamically buffered potentials in subsurface waters. *Geochim. Cosmochim. Acta* **68**, 4831–4842.

Williams, A.G.B., Scherer, M.M., 2004. Spectroscopic evidence for Fe(II)–Fe(III) electron transfer at the iron oxide-water interface. *Environ. Sci. Technol.* **38**, 4782–4790.

Zachara, J.M., Fredrickson, J.K., Smith, S.C., Gassman, P.L., 2001. Solubilization of Fe(III) oxide-bound trace metals by a dissimilatory Fe(III) reducing bacterium. *Geochim. Cosmochim. Acta* **65**, 75–93.

Zhang, T.C., Pang, H., 1999. Applications of microelectrode techniques to measure pH and oxidation–reduction potential in rhizosphere soil. *Environ. Sci. Technol.* **33**, 1293–1299.

Zibilske, L.M., 1994. Carbon mineralization. In: Weaver, R.W. (Ed.), Methods of Soil Analysis, Part 2. Microbiological and Biochemical Properties, vol. 5. Soil Science Society of America, pp. 835–863.